JGR Atmospheres

RESEARCH ARTICLE
10.1029/2022JD037450

Key Points:

- High convective available potential energy enhances non-inductive charging due to augmentation of ice-phase particle through dynamic process
- Elevated aerosol under low atmospheric instability conditions enhances lightning due to larger graupel participating in electrification
- An anomalous charge structure appears under polluted conditions, owing to positively charged graupel

Supporting Information:

Supporting Information may be found in the online version of this article.

Correspondence to:

X. Qie,
qiex@mail.iap.ac.cn

Citation:

Sun, M., Qie, X., Mansell, E. R., Liu, D., Yair, Y., Fierro, A. O., et al. (2023). Aerosol impacts on storm electrification and lightning discharges under different thermodynamic environments. *Journal of Geophysical Research: Atmospheres*, *128*, e2022JD037450. https://doi.org/10.1029/2022JD037450

Received 6 JUL 2022
Accepted 24 MAR 2023

Author Contributions:

Conceptualization: Mengyu Sun, Edward R. Mansell
Funding acquisition: Xiushu Qie, Yoav Yair
Methodology: Mengyu Sun, Edward R. Mansell
Validation: Xiushu Qie
Writing – review & editing: Xiushu Qie, Dongxia Liu, Yoav Yair, Alexandre O. Fierro, Shanfeng Yuan, Jingyu Lu

Aerosol Impacts on Storm Electrification and Lightning Discharges Under Different Thermodynamic Environments

Mengyu Sun[1,2,3], Xiushu Qie[1,3], Edward R. Mansell[4], Dongxia Liu[1], Yoav Yair[5], Alexandre O. Fierro[6], Shanfeng Yuan[1], and Jingyu Lu[1,3]

[1]Key Laboratory of Middle Atmosphere and Global Environment Observation, Institute of Atmospheric Physics, Chinese Academy of Sciences, Beijing, China, [2]State Key Laboratory of Remote Sensing Science, College of Global Change and Earth System Science, Beijing Normal University, Beijing, China, [3]College of Earth and Planetary Sciences, University of Chinese Academy of Sciences, Beijing, China, [4]NOAA/National Severe Storms Laboratory, Norman, OK, USA, [5]School of Sustainability, Reichman University, Herzliya, Israel, [6]Zentralanstalt für Meteorologie und Geodynamik, Department of Forecasting Models-ZAMG, Vienna, Austria

Abstract The impacts of aerosol and thermodynamics on electrification and lightning activities have been investigated in detail using the Weather Research and Forecasting Model coupled with a double-moment microphysics parameterization and an explicit electrification lightning scheme. To obtain a varied combination of convective available potential energy (CAPE) values and aerosol concentrations, a sounding was modified consistently and initiated with five sets of aerosol concentrations that served as cloud condensation nuclei. The simulated electric processes respond to the varying dynamical and microphysical characteristics associated with the different CAPE and aerosol conditions. Under high CAPE circumstances, the augmentation of ice-phase particle leads to the enhancement of non-inductive charging primarily through the dynamic processes. Increased aerosol content further invigorates the electrification through microphysical processes. Elevated aerosol loading under low CAPE conditions increases cloud droplet and ice crystal numbers. Larger graupel particle size further leads to the enhanced electric intensity and lightning discharges.

Plain Language Summary A weather forecast model with an embedded lightning scheme was used to investigate the effects of aerosol and atmospheric conditions on electrification and lightning activity. Varied combinations of moisture and temperature profiles and aerosol concentration were considered in the simulations. The results showed that the electrification and lightning activity vary under different meteorological and aerosol conditions. Under high convective available potential energy (CAPE) conditions, the increased ice-phase particle content leads to the enhancement of rebounding ice collisions mainly through the dynamic processes. Elevated aerosol loading under lower CAPE conditions invigorates lightning activity due to larger graupel particles participating in the thunderstorm electrification.

1. Introduction

Lightning activity is generally regarded to be invigorated with elevated aerosol loads (Li et al., 2019; Sun et al., 2021; Westcott, 1995), although excessive aerosol particles may lead to inhibition of convection and reduction of lightning activity (Altaratz et al., 2010; Mansell & Ziegler, 2013). Added aerosols increase the cloud droplet number and delay rain formation (Rosenfeld et al., 2008), then the updrafts lift more liquid hydrometeors to the mixed-phase region, where the increased latent heat of freezing helps to sustain the greater mass loading. Ultimately, the increased supercooled water and ice-phase particle content affect the charge separation and lightning activity via non-induction electrification mechanism (Takahashi, 1978; Yair et al., 2021). Thornton et al. (2017) found that lightning is enhanced by about a factor of 2 directly over two of the world's busiest shipping lanes, related to elevated ship exhaust particles. This may be considered as a proof for an indirect effect of aerosols on the microphysics of thunderstorms. Similar results were reported by Hu et al. (2019) in the Houston region and by Yuan et al. (2011) over the West Pacific Ocean east of the Philippines.

The simultaneous impacts of thermodynamics and aerosols result in a complex response of lightning to increased aerosols (Berg et al., 2008; Stolz et al., 2015; Zhao et al., 2020). Utilizing observational datasets, Wang et al. (2018) showed that lightning frequency is much higher in moist central Africa than in the drier northern region and has a "boomerang shape" with a saturation effect around an aerosol optical depth (AOD) of 0.3. As AOD exceeds the threshold, the response turns to be negative and is more pronounced in

Table 1
Basic Configuration and Physical Parameterizations for the Model Simulations

Parameter	Model option chosen
Horizontal domain Coverage	200 km × 200 km
Horizontal grid spacing	$dx = dy = 0.5$ km
Vertical levels	40
Time step	3 s
Duration of model runs	6 hr
Microphysics Scheme	NSSL 2-moment
Boundary Layer Scheme	BouLac PBL
Land Surface Scheme	Unified Noah LSM

the northern African region, presumably due to the combined influences of aerosol and different thermodynamics [for example, convective available potential energy (CAPE) and relative humidity (RH)]. Liu et al. (2021) found that increased aerosol in moist oceanic convection enhanced lightning discharges during the 2019–2020 Australian wildfire episode, owing to the augmentation of smaller ice particles and robust mixed-phase development. Observational data is limited by its inability to provide detailed in-cloud pictures of the ice-phase microphysics (e.g., graupel, ice crystals), making it challenging to directly study the aerosol effects on microphysical and electrical processes.

Previous numerical simulations have examined the relative effects of aerosols and thermodynamics on convective cloud properties. Fan et al. (2007) found that the aerosol effect on the trade cumulus clouds depended on RH and vertical wind shear, with greater significance in humid air. However, Storer et al. (2010) indicated that changes in cloud droplet, raindrop, and ice water were more sensitive to the aerosol loading, compared to the thermal conditions (i.e., CAPE). Furthermore, the simulated multicell storm in Mansell and Ziegler (2013) showed that increased condensation, graupel mass, and ice crystal production as cloud condensation nuclei (CCN) concentration was altered from 50 to >500 cm^{-3} in conditions with intermediate warm cloud depth (the vertical distance from the lifted-condensation level to the freezing level). They also noted that greater CCN concentrations enhanced peak updraft and lightning activity, but dropped again at extremely high CCN concentration (>2,000 cm^{-3}) owing to the reduced rime ice splintering. Few studies have discussed the aerosol effects on cloud microphysical processes and associated electrification in varying environments, with sophisticated microphysics and charging schemes in the model (e.g., Mitzeva et al., 2006; Takahashi, 1984). How to distinguish the detailed impacts of aerosols and thermodynamics on storm electrification through modeling study remains a challenge.

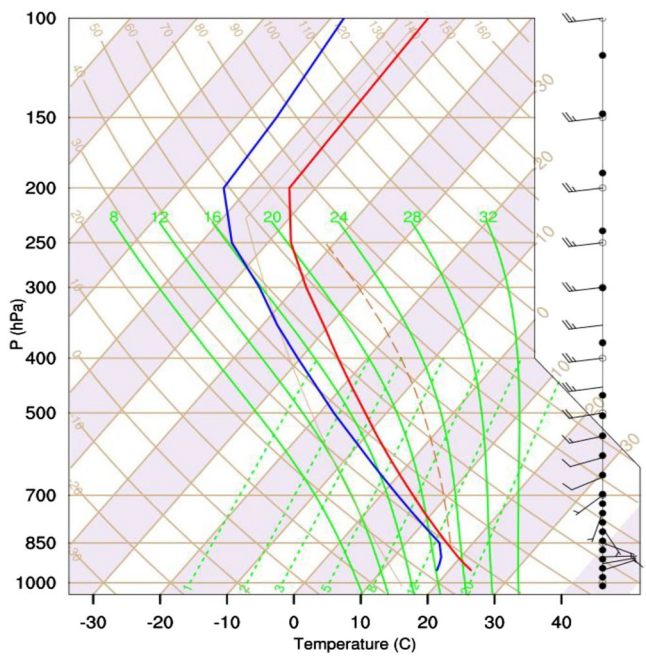

Figure 1. The sounding used to initialize the simulations at surface mixing ratio of 14 g kg^{-1} (Weisman & Klemp, 1982).

Table 2
Naming Conventions for the Sensitivity Experiments

Surface mixing ratio ($g\ kg^{-1}$)	CCN concentration (cm^{-3})				
	400	800	1,600	3,200	6,400
10	A-400	A-800	A-1600	A-3200	A-6400
12	B-400	B-800	B-1600	B-3200	B-6400
14	C-400	C-800	C-1600	C-3200	C-6400
16	D-400	D-800	D-1600	D-3200	D-6400

This study seeks to investigate the impacts of CCN concentrations on charge separation and lightning discharges under varying environments, via idealized modeling experiments. Different combinations will be adopted to evaluate the effects of both CCN and CAPE. This paper includes the following parts: Section 2 describes the methodology and the design of simulations, Section 3 presents the results, and Section 4 provides conclusions and discussions.

2. Methods

2.1. Model Description

A version of the Weather Research and Forecasting (WRF) Model (3.9.1.1; Skamarock et al., 2008) with explicit electrification (WRF-ELEC; Fierro et al., 2013) is used for this study. WRF-ELEC includes graupel-ice noninductive charging parameterization (Mansell et al., 2005) and a simplified local lightning discharge scheme (Fierro et al., 2013).

The NSSL microphysics scheme (Mansell et al., 2010) predicts the mixing ratio, number concentration, and electric charge of each hydrometeor species (i.e., cloud droplets, raindrops, ice crystals, snow, graupel, and hail). The deposition of water vapor, collection of supercooled water droplets, capture of ice particles, and collection of snow particles are all considered for the graupel growth. More detailed interactions and conversions among particles can be found in Mansell et al. (2010). The aerosol (representing with CCN) number concentration is set as a bulk activation spectrum, following Equation 1:

$$N_{\mathrm{CCN}} = \mathrm{CCNC} \times S^{k} \tag{1}$$

with CCNC is the assumed CCN concentration, S is the supersaturation, and k is arbitrarily set to 0.6 (Mansell et al., 2010). The cloud droplets are activated by the model according to Twomey (1959). The model tracks the unactivated CCN, and the local CCN concentration is depleted when droplets are activated. The CCN are subjected to advection and subgrid turbulent mixing, but have no other interactions with hydrometeors (e.g., CCN are not scavenged by hydrometeors; Mansell & Ziegler, 2013).

In this study, explicit charging (Mansell et al., 2005) includes both non-inductive and inductive (or polarization) charging mechanisms. Non-inductive charging, which is independent of pre-existing electric field, is based on rebounding collisions of ice particles (e.g., ice crystal, graupel) in the presence of supercooled liquid water. The non-inductive electrification scheme herein is adapted from Saunders and Peck (1998). The inductive charging (i.e., dependent on external electric field) is also taken into account because it can be crucial for lower charge region (Mansell et al., 2010; Zhao et al., 2010). The electric potential is obtained through the MPI black box multigrid solver (Dendy, 1987), from which the field vector E field is computed.

The discharge scheme is used within a cylindrical volume surrounding each lighting initiation point, which extends vertically through the depth of the domain (Fierro et al., 2013). The lightning initiation points are defined as grid cells where the electric field magnitude E_{mag} surpasses a critical breakdown threshold E_{crit} (Dwyer, 2003). A charge reduction of 30% (Ziegler & MacGorman, 1994) is applied within a column of prescribed radius of $R = 12$ km centered at each initiation point, following Fierro et al. (2013). At a given time step, the discharge is repeated iteratively until the maximum E_{mag} is less than the E_{crit} anywhere in the domain. An estimation of lightning flash rate within a domain of D (during an interval $T = t_2 - t_1$) is defined as follows:

$$\mathrm{LFR}(D,T) = \sum_{(i,j)\in D}\left[\frac{G}{C}\int_{t_1}^{t_2} B(i,j,t)dt\right], \tag{2}$$

with G is the area of horizontal grid, C is the cross-section area of the cylinder. The integral describes the total discharges $[B(t)]$ in the interval T.

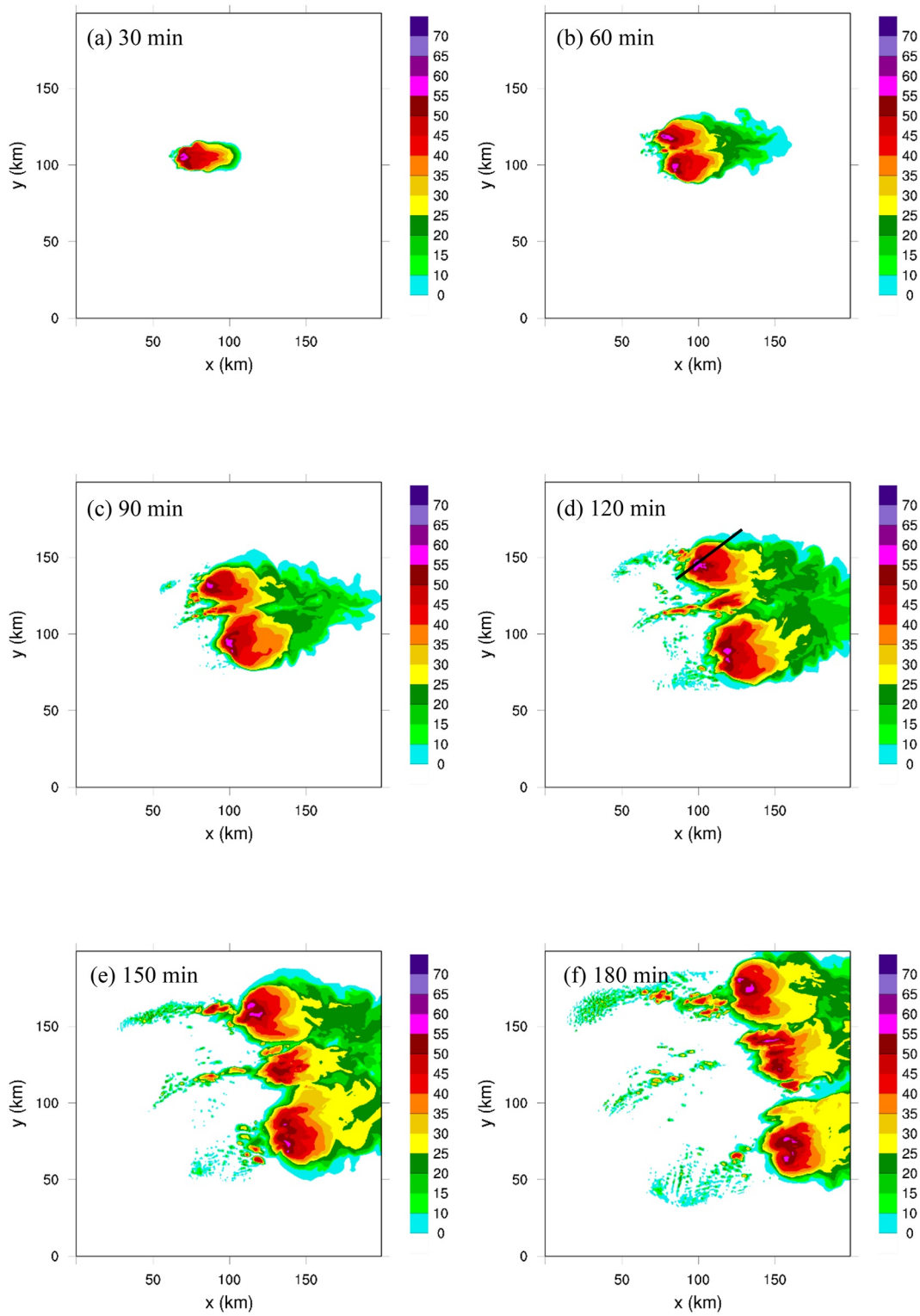

Figure 2. Time series of radar reflectivity (unit dBZ) of simulation A-400. (a) 30 min, (b) 60 min, (c) 90 min, (d) 120 min, (e) 150 min, (f) 180 min.

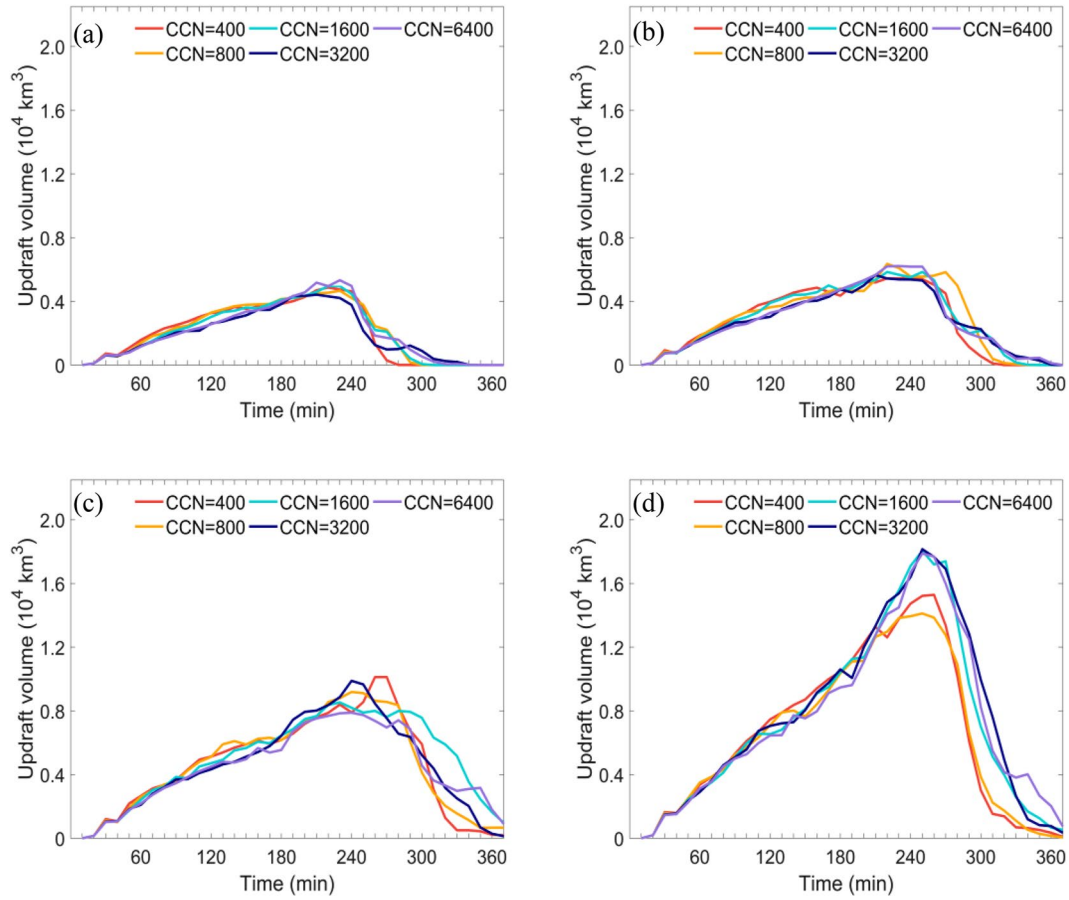

Figure 3. Temporal evolution of 5 m s^{-1} updraft volume for the different surface mixing ratios. (a) A, (b) B, (c) C, (d) D. The red, orange, blue, navy blue and purple lines correspond to the different cloud condensation nuclei concentrations of 400, 800, 1,600, 3,200, and 6,400 cm^{-3}.

2.2. Design of the Simulations

The simulations were triggered by horizontally homogeneous but vertically different soundings. Table 1 shows a summary of the WRF-ELEC model settings. The domain has a horizontal resolution of 0.5 km (400 × 400 grid points). The top is set to be 50 hPa with 40 vertical levels. In order to obtain a full picture of the convection, the simulations were integrated up to 6 hr. The thermodynamic profile used for the control simulation is presented in Figure 1, following Weisman and Klemp (1982) to represent a continental deep convective storm environment. This profile has surface water vapor mixing ratio (Qv) and RH of 14 g kg^{-1} and 70%, respectively, and a surface-based CAPE of 1,900 J kg^{-1}. A moderate vertical wind shear was used to produce convection of longer lifetime (Seifert & Beheng, 2006; Storer et al., 2010), making it possible to study the effects of aerosols and thermodynamics on long-lived storms. To examine the sensitivity of CAPE, the boundary layer Qv was modified in the original sounding from 10 to 16 g kg^{-1} by increments of 2 g kg^{-1} to obtain different pre-storm environments, which is a similar range as Seifert and Beheng (2006) and Storer et al. (2010). The CAPE increases with added surface Qv, with the values of 276, 1,010, 1,900 and 3,100 J kg^{-1} at Qv = 10, 12, 14, 16 g kg^{-1}. Over the lowest 750 m, Qv was assumed constant to represent a well-mixed boundary layer, following Weisman and Klemp (1982) and Storer et al. (2010). Changes in CAPE have also been achieved by altering the temperature profile. But previous tests suggested that the qualitative results are insensitive to at least minor changes in the above profile (Weisman & Klemp, 1982).

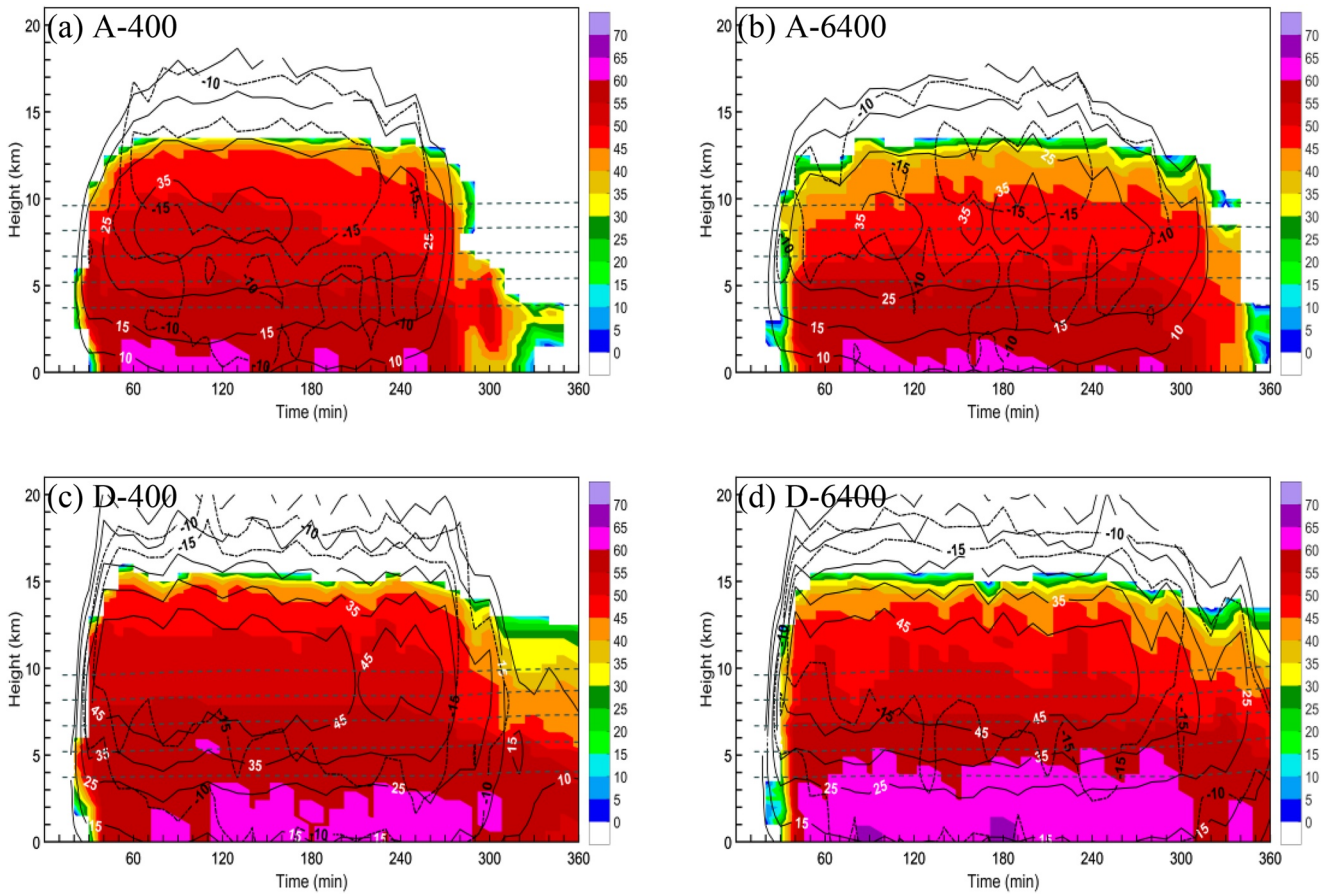

Figure 4. Temporal evolution of the horizontal maximum radar reflectivity (shaded, unit dBZ) and vertical velocities (solid line: 10, 15, 25, 35, 45 m s^{-1}; dashed line: −10, −15 m s^{-1}) for the model run (a) A-400, (b) A-6400, (c) D-400, (d) D-6400. The 0, −10, −20, −30 and −40°C isotherms are represented by the dashed lines.

To examine the impacts of CCN concentration on the storm structure and lightning activity in different thermodynamic environments, four sets of simulations were carried out with a wide range of CCN concentrations: 400, 800, 1,600, 3,200, and 6,400 cm^{-3}. The CCN concentration of 400 cm^{-3} was chosen to represent a relatively pristine continental condition, and the value of 6,400 cm^{-3} was selected for a highly polluted case (Mansell & Ziegler, 2013; Sun et al., 2021). The charge separation required for lightning formation are resulted from the collisions between ice-phase particles in the presence of supercooled water (e.g., Saunders & Peck, 1998; Takahashi, 1978). In order to investigate the aerosol effects upon lightning activity, high CCN concentrations were prescribed to guarantee the small droplet sizes and make the ice process dominant for precipitation formation (Mansell et al., 2005). The cloud droplets of small diameters should effectively turn off the warm rain process (Dye et al., 1974). The local CCN concentration is defined as $N\times(\rho_{air}/\rho_0)$ cm^{-3}, where $\rho_0 = 1.225$ kg m^{-3} is the sea level air density and N/ρ_0 is the initial number mixing ratio. Table 2 shows the combinations of surface Qv and initial CCN concentration for the sensitivity experiments. The corresponding naming conventions are also shown in Table 2, among which the letters A-D represent varied values of surface Qv.

3. Results

3.1. Simulation of the Storm Development

The simulations produced comparable developments of the storm. Figure 2 presents the time series of radar reflectivity of the A-400 case (i.e., lowest CCN concentration and lowest CAPE). Around 60 min into the simulation, the storm splits into two separate cells, of which the right one persists for the entire duration of the storm. The left cell slowly develops into widespread multicellular convection after the initial split. These developments

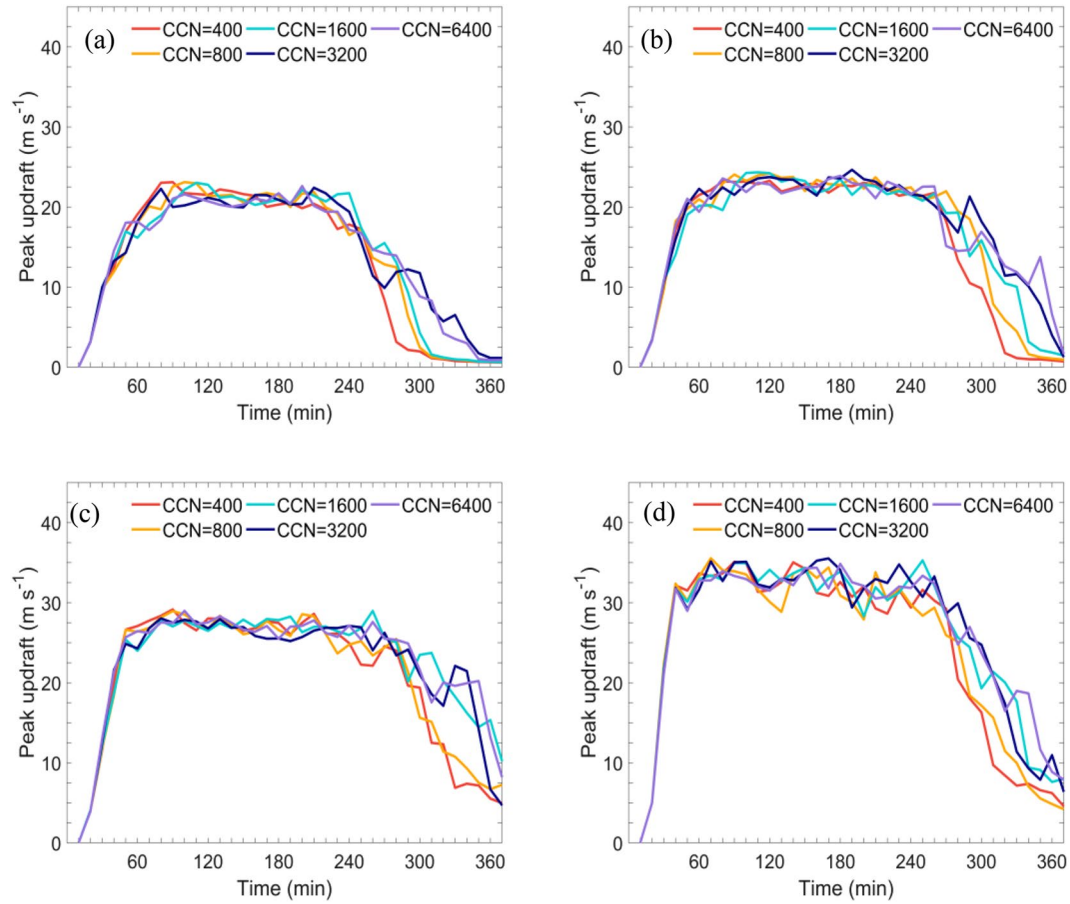

Figure 5. Temporal evolution of domain-averaged maximum updraft speed (m s^{-1}) for the different surface mixing ratios. (a) A, (b) B, (c) C, (d) D. The red, orange, blue, navy blue, and purple lines correspond to the different cloud condensation nuclei concentrations of 400, 800, 1,600, 3,200, and 6,400 cm^{-3}.

are similar to the observed and simulated studies (e.g., Storer et al., 2010; Weisman & Klemp, 1984). Some noteworthy differences occur in storm strength and duration, however, due to the varied thermal conditions and CCN concentrations.

As shown in Figure 3, the updraft volume (threshold of 5 m s^{-1}) is dramatically affected by the CAPE. Increasing the CAPE (from 276 to 3,100 J kg^{-1}) leads to an enhancement of the updraft volume up to ~260%. The highest volume of updraft occurs at the very large value of CAPE (3,100 J kg^{-1}), corresponding to the extremely strong convection (Figure 4). The convection is less sensitive to CCN concentrations compared to thermal conditions, with similar updraft volume under comparable CAPE values (Figures 3 and 4). As the surface vapor mixing ratio reaches 16 g kg^{-1}, the aerosol effects on the updraft volume tend to be slightly more obvious (Figure 3d). With high CCN concentration, the increased latent heat release partially enhances the updrafts but is offset by increased mass loading (Rosenfeld et al., 2008; Williams et al., 2005). The differences of updraft volume between the higher CCN (1,600, 3,200, and 6,400 cm^{-3}) and the lower CCN concentrations (400 and 800 cm^{-3}), however, are still less than 20%. The increase in updraft volume is mainly attributed to the increased CAPE, and is less dependent on CCN.

For the lower CAPE cases, the maximum updraft has less pronounced CAPE dependence than the updraft volume. As shown in Figure 5, increasing the CAPE value from 276 to 1,010 J kg^{-1} leads to a <20% change in domain-averaged max updraft speed, increasing only from 22 m s^{-1} (CAPE value of 276 J kg^{-1}) to ~25 m s^{-1} (CAPE value of 1,010 J kg^{-1}). At a constant CAPE, when looking at changes due to CCN concentration, it can also be seen that the storms with increased CCN concentrations have similar maximum updraft speed, before 270 min (Figure 5). A substantial reduction in peak updraft was found by Li et al. (2008) at extremely high CCN

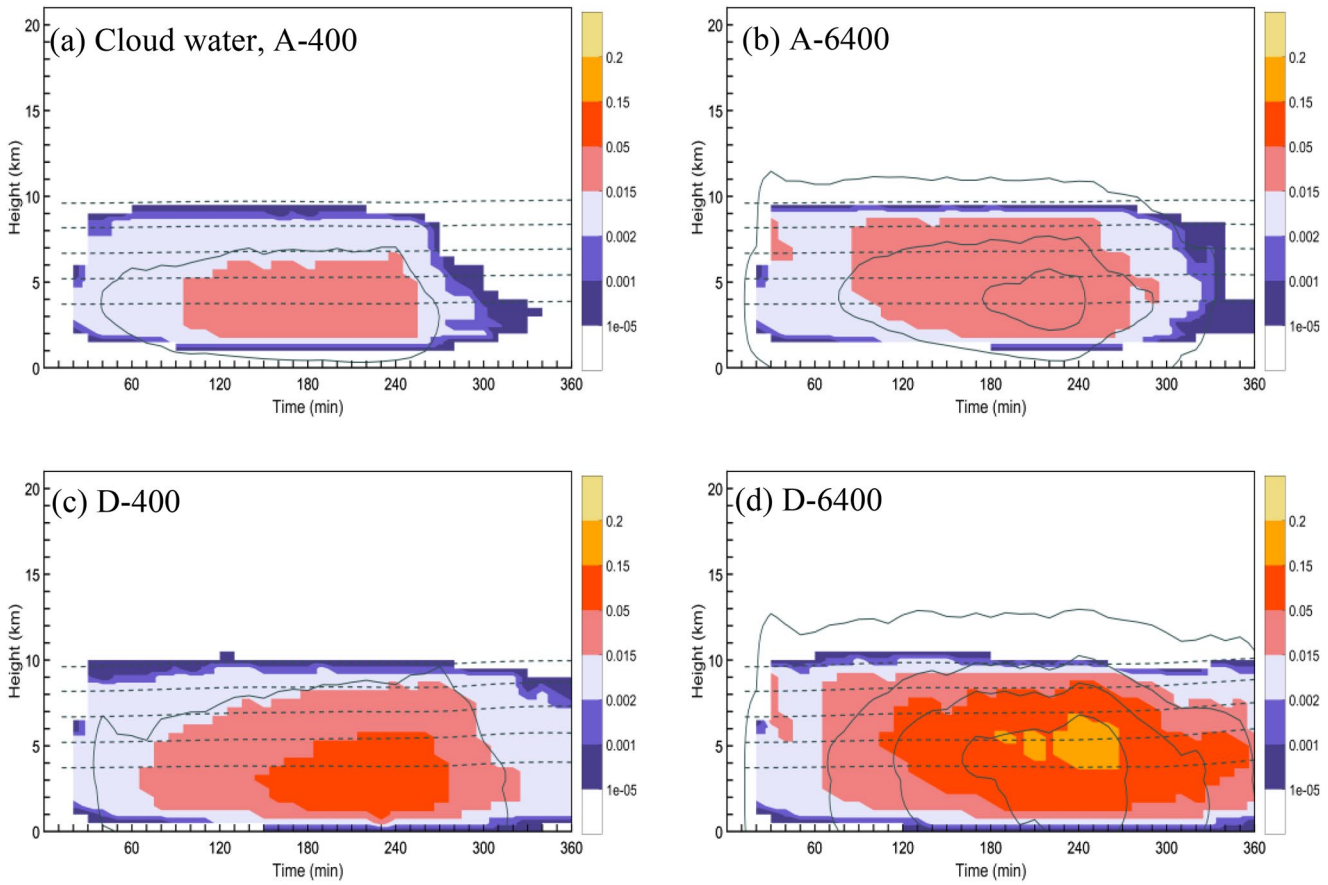

Figure 6. Temporal evolution of the horizontally domain-averaged mass mixing ratio (g kg^{-1}, shaded) and number concentration (kg^{-1}, solid line) of cloud water for the model run (a) A-400, (b) A-6400, (c) D-400, (d) D-6,400. Contour levels in (a–d) are 10^6, 2×10^7, 5×10^7, 10^8 kg^{-1} for the cloud droplet number concentration.

concentration (>5,000 cm^{-3}). Mansell and Ziegler (2013) showed no dramatic decrease in peak updraft speed under high CCN, which is more consistent with the result found in this study. Varied grid resolution and storm initialization could be the possible reasons for these differences (Bryan et al., 2003; Fierro et al., 2009). The duration of the convection in the study area is prolonged, especially in the lower CAPE cases (Figure 5a), mainly because the storms move more slowly and stay in the domain longer under polluted conditions.

3.2. Microphysical Properties of the Storm

As examples of how different the microphysical processes can be, Figures 6 and 7 depict the combinations of the lowest (highest) values of CAPE and CCN concentration (i.e., A-400, A-6400, D-400, and D-6400). Shown are the mass mixing ratio and number concentration of various hydrometeors. These properties are averaged horizontally over the cloudy grid points (those without zero values) at each given altitude. As shown in Figure 6, the increasing CAPE leads to dramatic increases in the mixing ratio of cloud droplet, as is the case for the number concentration. The responses of the number concentration and mean-mass radius of hydrometeors, which are averaged spatially and temporally over cloudy grid points, are presented in Figure 8. It can be seen that the dynamic-thermodynamics effects on properties of cloud droplets and rain drops are especially significant in the higher CAPE cases (1,900 and 3,100 J kg^{-1}, Figures 8a and 8c). Enhanced CAPE will be transformed into differences in dynamic characteristics (i.e., vertical velocity), which could further influence the activation of aerosol as CCN due to the increased supersaturation created by the stronger updrafts. The aerosol impacts on the cloud microphysics are dependent on CAPE, and these impacts become more pronounced in the higher CAPE conditions (Figures 6b and 6d).

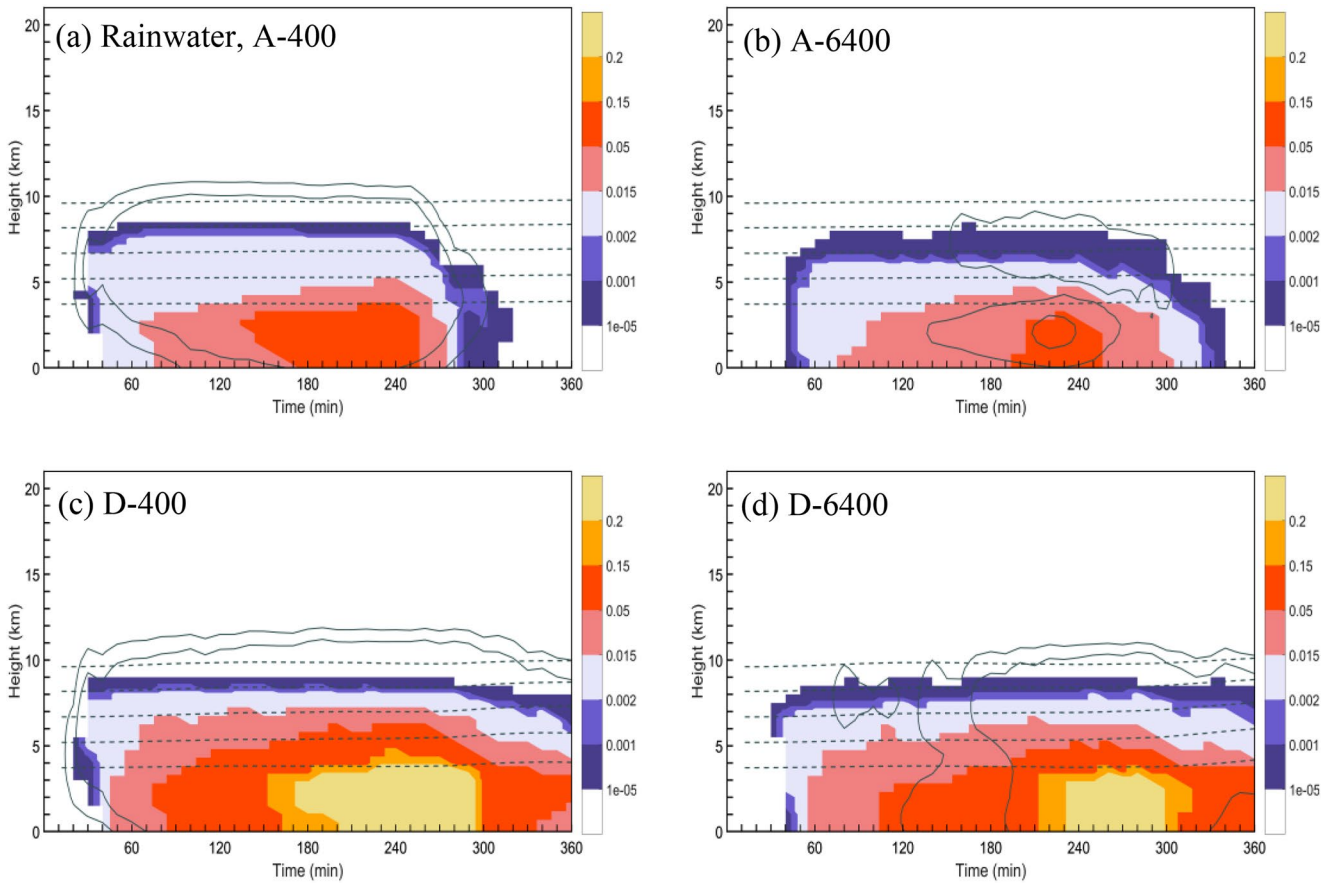

Figure 7. As in Figure 6, but for the rain water. Contour levels in (a–d) are 100 and 300 kg^{-1} for the rainwater number concentration.

For the polluted cases, the increase in CCN concentration increases droplet concentration and decreases droplet radius (Lynn et al., 2020; Sun et al., 2021; Yair et al., 2010; Figure 8a). Cloud droplets with smaller radius suppress the collection-coalescence processes. Thus, the rainwater content decreases with the added CCN (Figures 7b and 8c), particularly above the 0°C level. Those small droplets ascend in updrafts and continue growing, leading to an increase in supercooled cloud water content (CWC; Figures 6b and 6d). Smaller cloud droplets lifted to higher levels (above 8 km) will generate more ice particles in the upper glaciated region by homogeneous freezing of these droplets. From Figure 9b, it can be seen that the increased CCN concentration leads to the increase of ice crystal mixing ratio, even at the lowest CAPE value. Enhanced microphysical processes will increase the latent heat from both condensation and freezing, in turn boosting updraft velocities.

The size of raindrops is more dependent on the CCN concentration, as shown in Figure 8d. The raindrop size is larger in polluted conditions. The less efficient coalescence of cloud droplets could probably be compensated by the melting of larger amounts of ice-phase particles, leading to a larger raindrop size under polluted conditions. Figure 10 displays the temporal variation of volumetric precipitation in different conditions. It is obvious that storms with higher CAPE produce more precipitation. Under the same CCN concentration, the storm with the highest CAPE value forms more precipitation, which is about three times that is produced in the lowest CAPE condition. It should be noted that the accumulated precipitation is reduced in the most polluted case (6,400 cm^{-3}) under higher CAPE conditions (1,900 and 3,100 J kg^{-1}). This decrease in precipitation within the simulated scope of CCN concentration is ~20%.

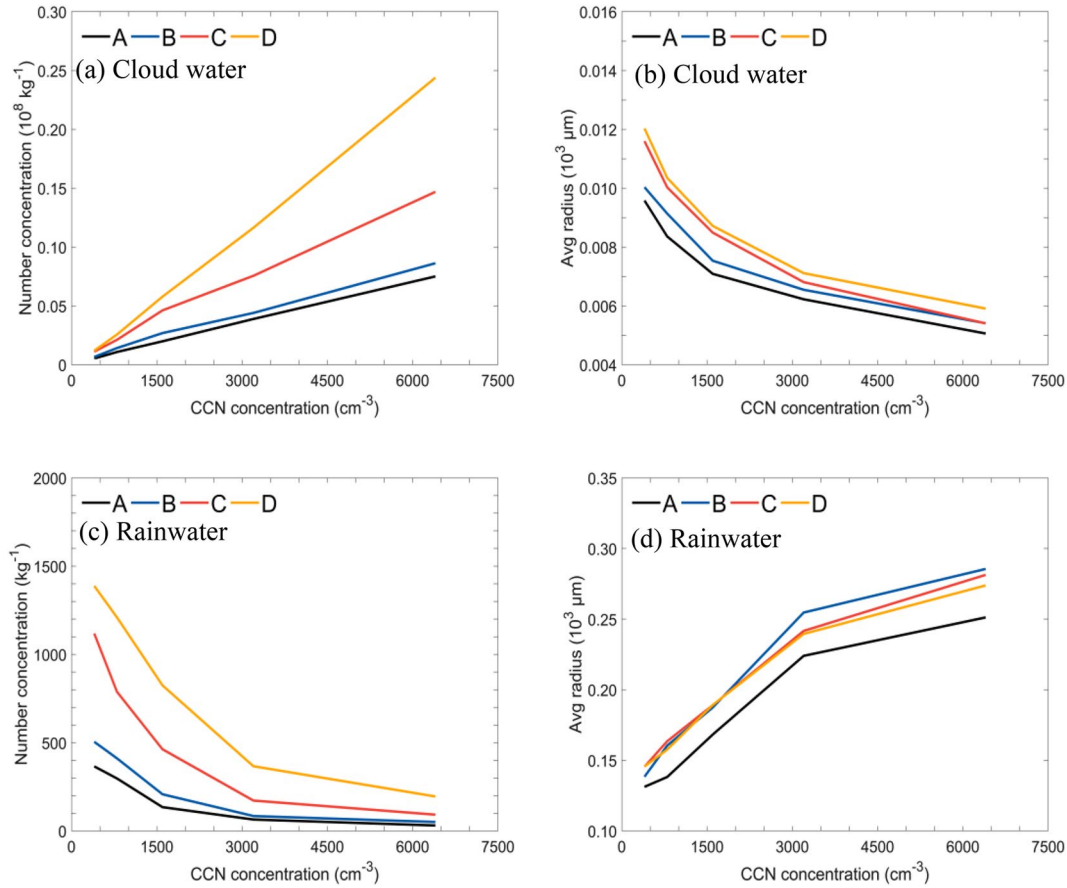

Figure 8. Domain-averaged (left) number concentration (kg^{-1}) and (right) mean-mass radius (10^3 μm) with respect to cloud condensation nuclei concentration for different species. (a, b) Cloud water, (c, d) rainwater. The black, blue, red and orange lines represent the different surface mixing ratios. (a) A, (b) B, (c) C, (d) D.

It is interesting to find that the initial CCN concentration and CAPE value have counteracting effects on the properties of graupel (Figure 11). Figure 12a shows that the graupel number concentrations increase with the increase of CAPE, however, the increased CCN concentration leads to a significant decrease in graupel content. With variable predicted graupel density in the simulations, the rime density increases during wet growth. The graupel volume is only allowed to increase at the minimum density (300 kg m^{-3}) when it collects ice crystals (Mansell et al., 2010). The increase in droplet freezing into cloud ice at high CCN concentration (Figure 9) is a reflection of reduced precipitation production, whether by warm rain processes or total accretion. Owing to more appreciable rainwater content and associated raindrop formation and freezing, the graupel mixing ratio increases under high CAPE conditions. It is clear that the maximum graupel concentration occurs in simulation D-400, with the lowest CCN concentration and the highest value of CAPE. Even in the highest CAPE case, the graupel number concentration still decreases with the added CCN concentration, indicating the impact of aerosol loading on the graupel number concentration. This might elucidate that the graupel particle size increases more dramatically with the increase of CCN concentration in the lower CAPE conditions (276 and 1,010 J kg^{-1}), compared to that at higher CAPE (1,900 and 3,100 J kg^{-1}, Figure 12b). Small hail could be represented by frozen drops in the graupel category, which has variable density (300–900 kg m^{-3}) in the microphysical scheme (Mansell et al., 2010). And the hail category, whose density is allowed from 500 to 900 kg m^{-3}, tends to represent larger hail resulting from the conversion of graupel when wet growth riming conditions exist (Milbrandt & Yau, 2005). The changes of properties of hail particle are similar to those of graupel, and its mean-mass diameter (range from about 0.25 to 0.5 cm, see Figure S5 in Supporting Information S1) is larger than that of graupel. The aggregation of snow is mainly through collecting droplets and cloud ice (Ziegler, 1985; Zrnic et al., 1993). Since there are more cloud water

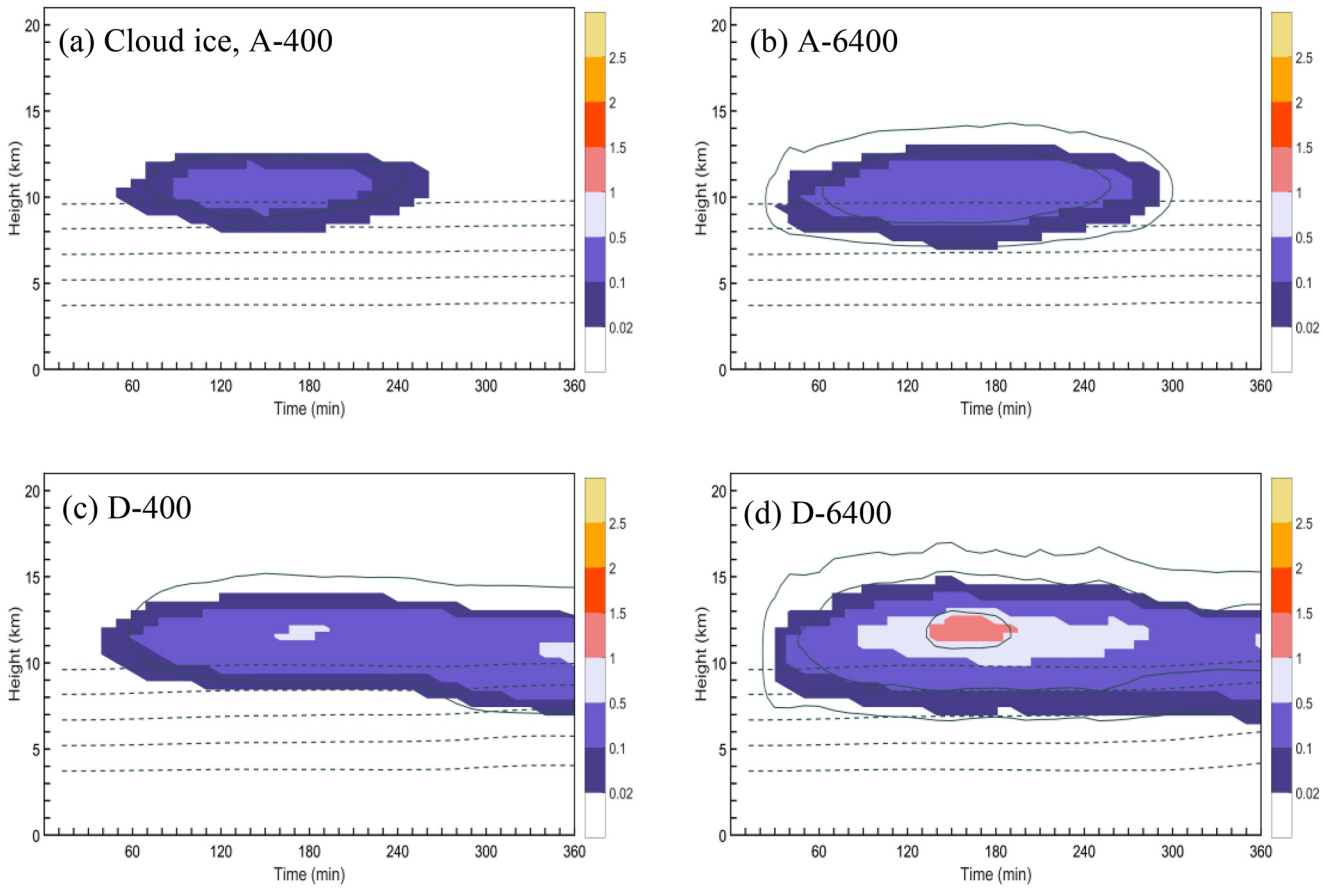

Figure 9. As in Figure 6, but for the cloud ice. Contour levels in (a–d) are 0.1×10^7, 1×10^7 and 5×10^7 kg^{-1} for the ice number concentration.

and ice crystals under polluted conditions, the snow content increases in simulations with higher CCN, so as the number concentration. Thus, the increases in the snow size (see Figures S4 and S6 in Supporting Information S1) are not as obvious as those of graupel. The strong dependence of these microphysical properties, particularly these of ice-phase particles, on the initial aerosol forcing, however, has not been thoroughly studied. Such changes in the microphysical processes could undoubtedly affect in-cloud electrification and discharges, whose impacts are expected to be more notable under low CAPE conditions (e.g., Mansell & Ziegler, 2013; Sun et al., 2021).

3.3. Electrification and Lightning

To illustrate how different the electrical processes can be, the vertical profiles of the charge density at different periods are shown in Figure 13. The combinations of the lowest (highest) values of the CAPE and CCN concentration are displayed. It is noted that the total charge density shown in Figure 13 is obtained by averaging horizontally (Fierro et al., 2013), which makes it possible for the sign of total charge density to represent the charge polarity at different levels. During each simulated period, it can be seen that CAPE has some variable effect on the maximum positive and negative charge densities. But it should be noted that these values are saved at the end of the time step after the lightning parameterization, which has reduced all electric field magnitudes below the initiation threshold. Therefore, the profiles in Figure 13 do not necessarily fully reflect differences in charging rates. A general charge structure with positive charge above the negative charge, which is classified as normal dipole (e.g., Thomas et al., 2001), is simulated during the entire simulated period (Figures 13a and 13b). And this is also the case in simulations A-400 and D-400 at various times (i.e., 120 min, 240 min), as shown in Figures 13c and 13e. Different from the cases of lower CCN, a negative charge center appears in upper levels (about 10 km), with a positive charge region located in the middle and a negative charge region in lower levels

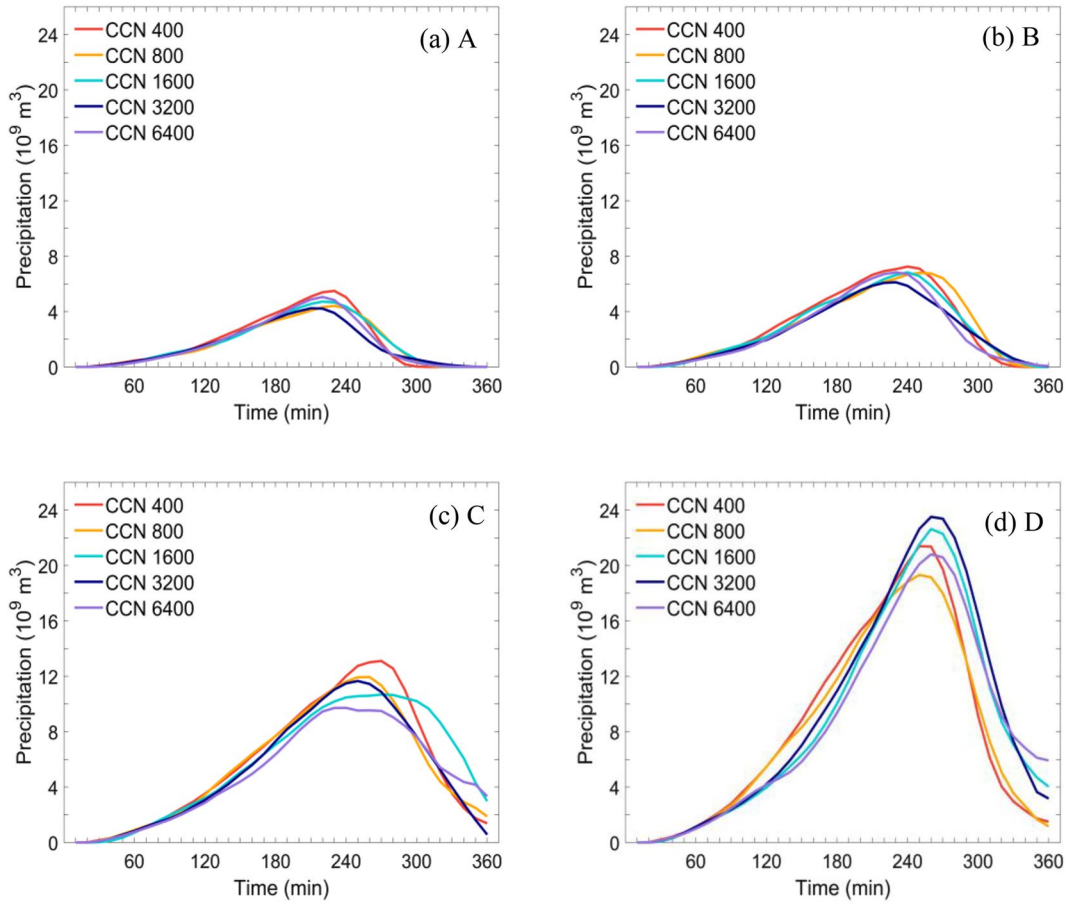

Figure 10. Temporal evolution of volumetric precipitation (10^9 m^3) at the different surface mixing ratios. (a) A, (b) B, (c) C, (d) D. The red, orange, blue, navy blue and purple lines correspond to the different cloud condensation nuclei concentrations of 400, 800, 1,600, 3,200, and 6,400 cm^{-3}.

(Figure 13d; e.g., Mansell et al., 2005; Eddy et al., 2021). Then the charge structure turns into a normal dipole, as shown in Figure 13f.

The charging rates, unlike the net charge densities, directly correspond to microphysical changes that affect the ice collision rates. In the simulations, the electrification mainly results from non-inductive charging (Mansell et al., 2005), which is caused by rebounding ice collisions (e.g., graupel, ice crystals). Its rate is about an order of magnitude higher than inductive charging (figure not shown; Mansell et al., 2010). Thus, only the changes of non-inductive electrification under various CAPE values and CCN concentrations will be discussed herein. The sensitivity of the peak non-inductive charging rate to the changes in CCN concentration and CAPE are presented in Figure 14. Some differences occur as a function of both. Either increased CAPE, or increased CCN concentration, can lead to the enhancement of non-inductive charging. Under the same CCN concentration, the peak non-inductive charging rates are 500 and 550 pC m^{-3} s^{-1} for the lower CAPE cases in A-6400 and B-6400, respectively. Increasing the CAPE (from 276 to 1,010 J kg^{-1}) results in an increase of charging rate less than 10% in the most polluted condition (6,400 cm^{-3}), which is much less than the increase of updraft volume caused by the change of CAPE (~30%). The change of peak non-inductive charging rate is about 350%, due to the increase of CCN concentration (from lowest to highest) with the highest CAPE value (Figure 14d). And with the lowest CAPE value, changing the CCN (from 400 to 6,400 cm^{-3}) brings about an increased peak non-inductive charging rate from 40 to 480 pC m^{-3} s^{-1} (Figure 14a). The electrical processes are arguably more sensitive to the available aerosol loading than to CAPE.

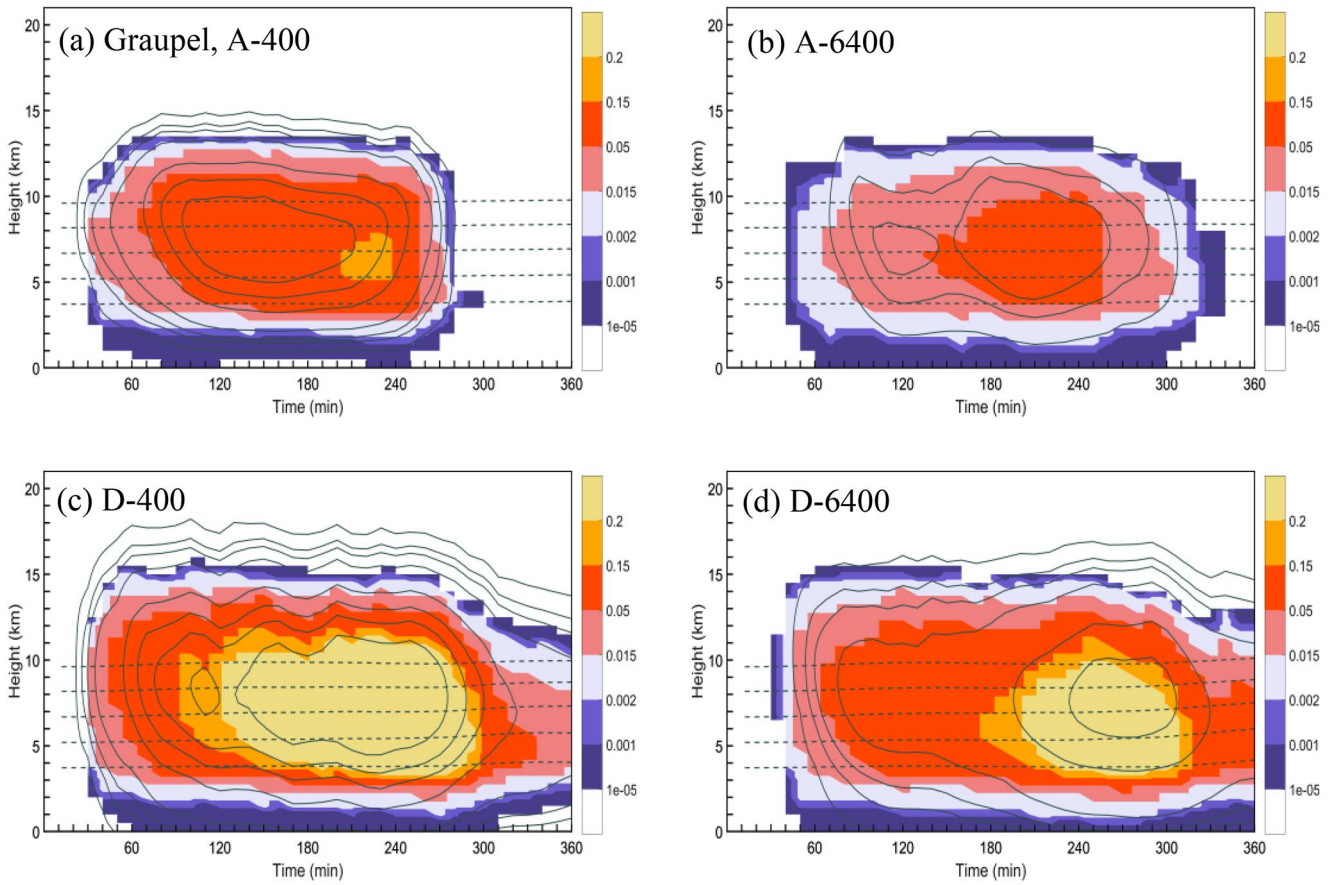

Figure 11. As in Figure 6, but for the graupel. Contour levels in (a–d) are 10, 30, 50, 100, 300, 500, 700, and 1,000 kg^{-1} for the graupel number concentration.

As the maxima of the peak non-inductive charging rate occurs at about 120 min (Figure 14), we further depicted the vertical profiles of non-inductive charging rate at this time. Since the charge separation parameterization primarily depends on graupel-ice collisions in mixed-phase updrafts (Mansell & Ziegler, 2013), the profiles of the charge carried by graupel and ice crystals are also shown in Figure 15. In the lowest CAPE (value of 276 J kg^{-1}) case, the maximum charging rate occurs at 8–10 km (Figure 15a), which corresponds to the upper positive charge center in the normal dipole structure. And as the CCN concentration is increased, the non-inductive charging rate increases significantly. In the corresponding levels (8–10 km), the graupel particles are primarily charged positively (Figure 15b), with ice crystals charged negatively. In the cases of lower CCN and highest CAPE, the graupel particles are charged negatively at ∼10 km and charged positively at lower levels (Figure 15e). Based on the non-inductive charging curve (Saunders & Peck, 1998), graupel can be charged negatively within regions of lower CWC at ∼10 km. In cases of higher CCN, graupel particles are charged positively with the existence of higher CWC and the reverse for ice crystals. Therefore, a negative charge center appears in upper levels (above 12 km) under polluted conditions, with a positive charge region located in the middle levels (Figure 13e). As shown in Figure 15b, the peak charge density of graupel particles is 0.2 nC m^{-3}, which is about twice that of ice crystals. Considering that the ice crystal content is notably less in these circumstances (lower CAPE values; Figure 12c) and hardly contributes to the non-inductive charging, the charged graupel particles thus play a vital role in the upper charge region. These graupel particles of larger radius account for an enhanced charging primarily owing to the higher collision-collection efficiency with other ice species (e.g., snow and hail particles).

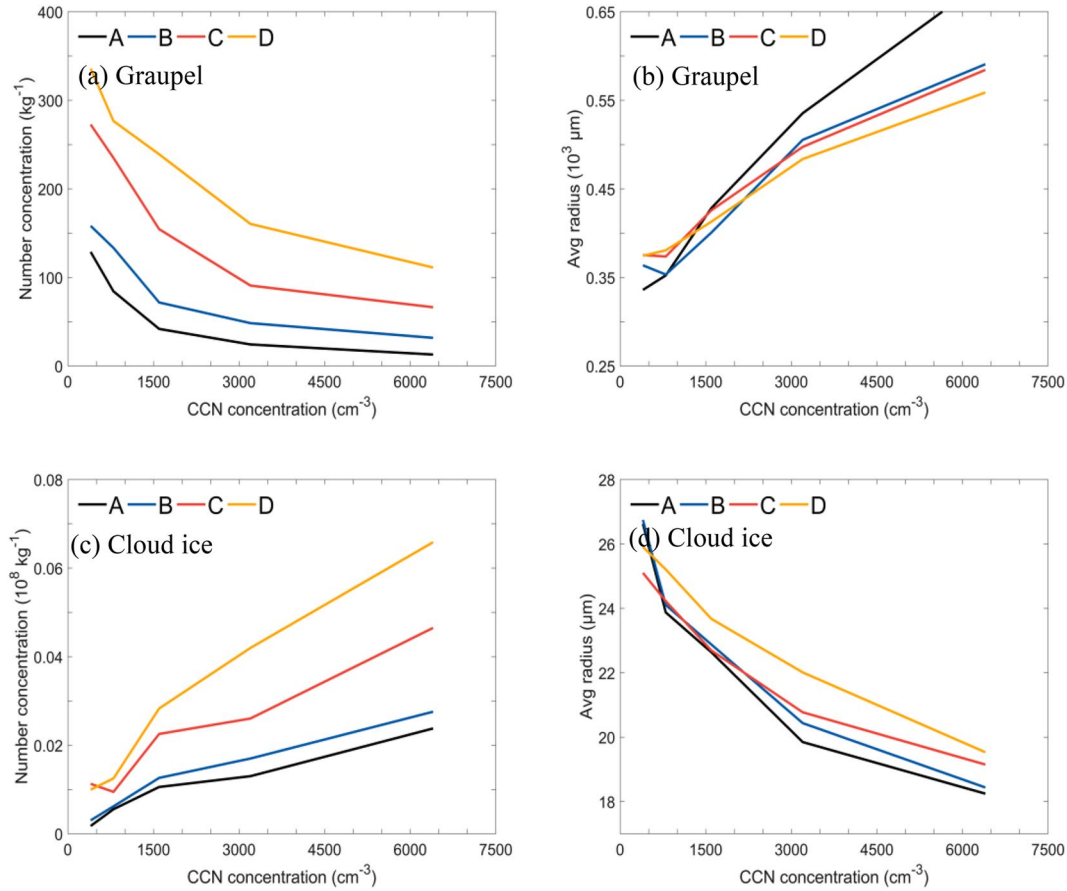

Figure 12. As in Figure 8 but for the (a, b) graupel and (c, d) cloud ice.

To investigate the relationship between hydrometeors and electrification under different CCN conditions (namely, A-400 and A-6400), vertical cross sections are shown in Figures 16 and 17. According to the non-inductive charging mechanism, the charge structure could vary among separate cells owing to the differences in updrafts and CWC (Saunders & Peck, 1998). These cross sections are chosen depending on the location of maximum value of radar reflectivity. The total charge density carried by different ice-phase particles is displayed at about 120 min. As shown in Figure 16a, the charge structure with positive charge above the negative charge exists in case A-400. This positive charge region (above 10 km) mainly results from the cloud ice and snow particles (Figure 16b). In case A-6400, a negative charge center appears in the upper level (>10 km) at this time, with a positive charge center in the middle and a negative charge center in lower levels (Figure 17a). This simulated vertical charge distribution is caused by ice and snow particles charged negatively at 8–12 km, and graupel and hail particles charged positively at 4–8 km (Figures 17b and 17d). As discussed above, more supercooled cloud droplets in upper levels (>10 km) probably explains the existence of positively charged graupel and the anomalous polarity charging at higher CCN. And the efficient collisions between graupel of larger size and other ice-phase particles (i.e., hail, snow and ice crystals) further lead to the intense positive charge center located at 8–10 km (Figures 17a and 17b). In caseA-6400, the maximum positive charge density at this time is up to +1 nC m^{-3}, which is much higher than that in the A-400 (less than +0.5 nC m^{-3}).

This enhanced non-inductive electrification leads to greater charge density and in turn reinforces the electric intensity, further underlining the significance of aerosol on the lightning discharges through microphysical processes under lower CAPE conditions. As shown in Figure 18a, the lightning flash rates increase with greater CCN concentration, even with the lowest CAPE value. The sensitivity of these electrical properties on the aerosol loading in the higher CAPE and shear conditions has not previously been demonstrated in model simulations.

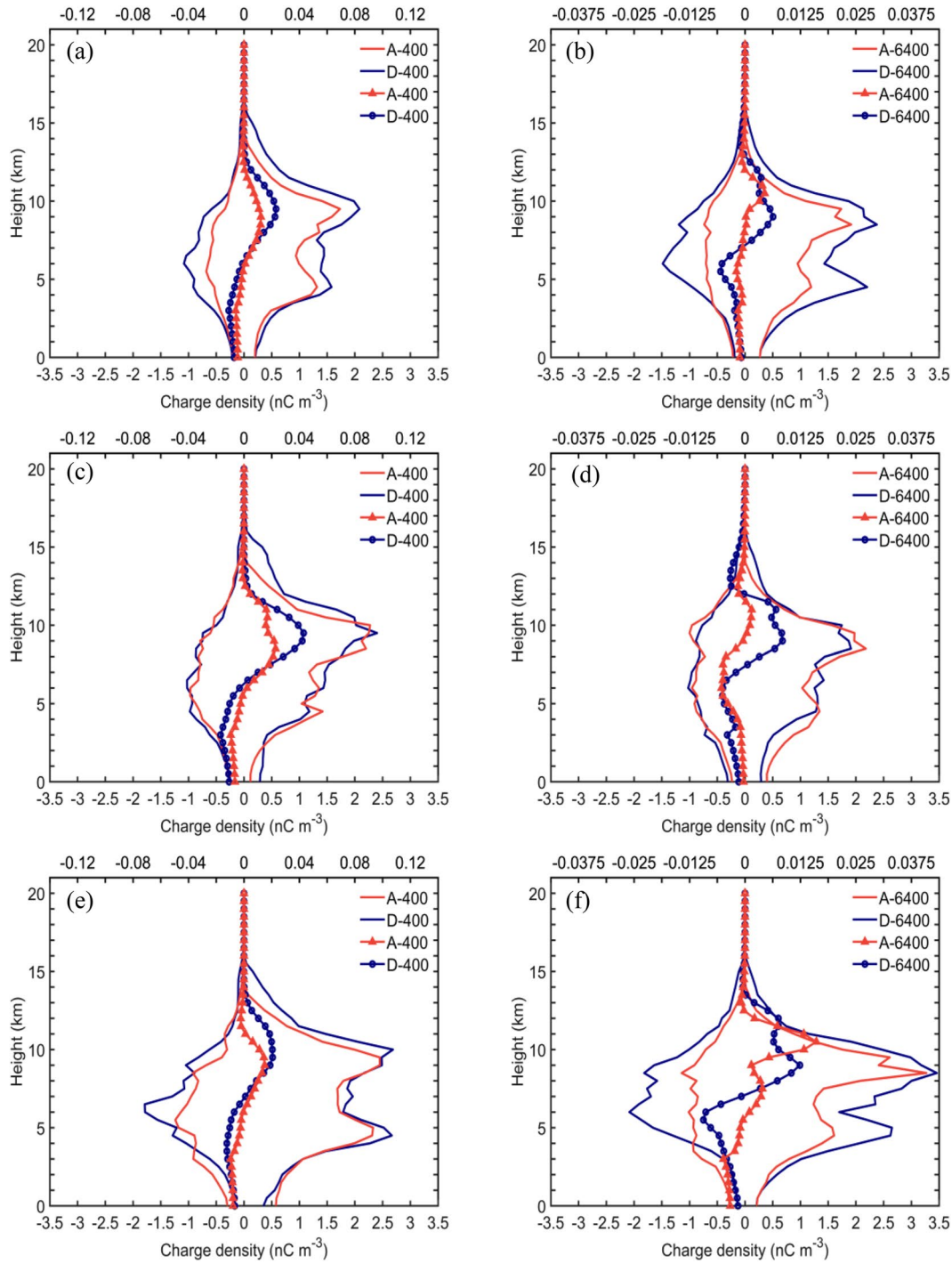

Figure 13. Vertical profiles of peak charge density (solid lines, nC m^{-3}) and domain-averaged after-discharging total charge density (marked lines, nC m^{-3}) for different cloud condensation nuclei concentrations at various periods. (a) 400 cm^{-3}, (b) 6,400 cm^{-3} during the entire simulated period, (c) 400 cm^{-3}, (d) 6,400 cm^{-3} at 120 min, (e) 400 cm^{-3}, (f) 6,400 cm^{-3} at 240 min. The red and blue lines correspond to the different surface mixing ratios of A and D. The *x* axis above is for the averaged values; the *x* axis below is for the maximum values.

As the CAPE value increases, the ice-phase particles increase, resulting in a significant increase in charging rate (Figure 14d) and charge density (Figure 13). The increase of charge density leads to the enhancement of electric processes and subsequent lightning discharges (Figure 18d). Liu et al. (2021) found that added aerosol could lead to a greater number of smaller-size ice crystals above the freezing level, consequently boosting lightning

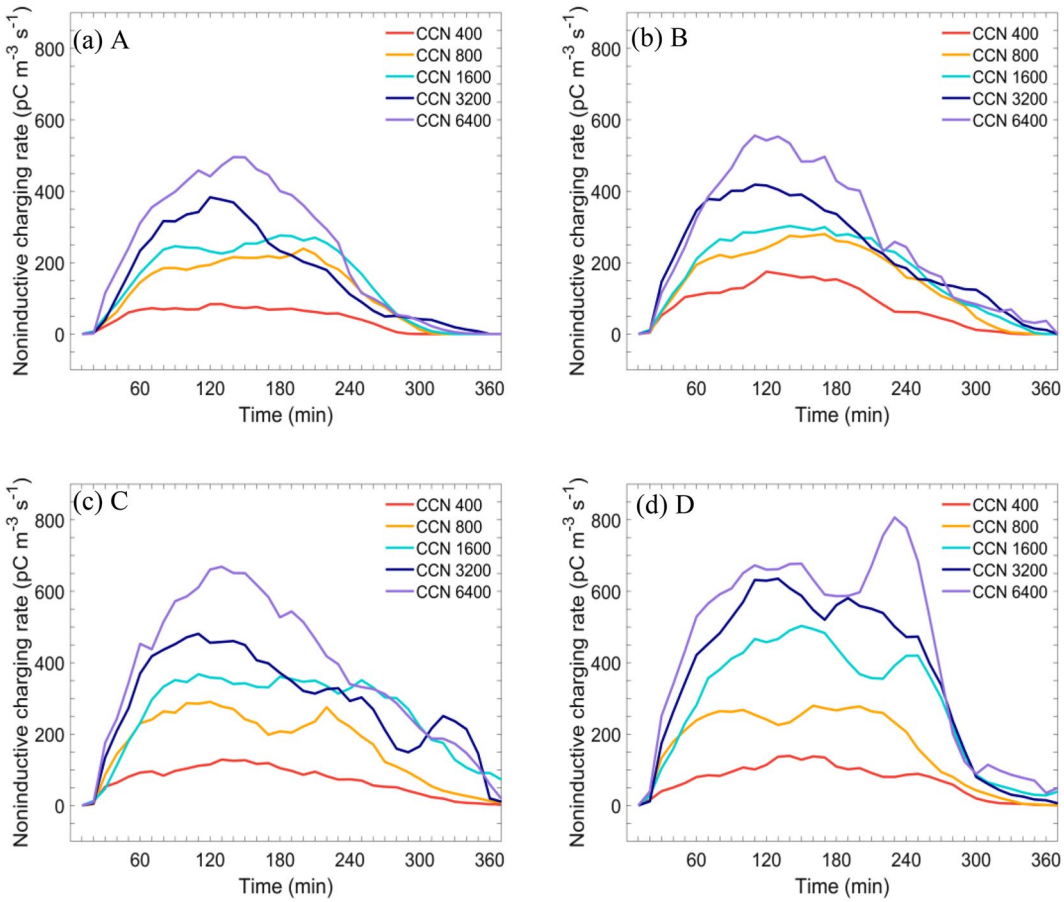

Figure 14. Temporal evolution of peak positive non-inductive charging rate (pC m^{-3} s^{-1}) at different surface mixing ratios. (a) A, (b) B, (c) C, (d) D. The red, orange, blue, navy blue and purple lines correspond to the different cloud condensation nuclei concentrations of 400, 800, 1,600, 3,200, and 6,400 cm^{-3}.

flash rates in oceanic convection. Our simulations support this hypothesis, that is, the augmentation of ice crystal content significantly increases the charge density. In this study, we also demonstrate that elevated aerosol concentration under low CAPE conditions leads to increased charge density, electric field magnitude and lightning activity, primarily resulting from the graupel of larger radius. Under high CAPE circumstances, added aerosol concentration further enhances the microphysical processes, leading to a more strengthened non-inductive charging, which in turn invigorates lightning flash rates.

4. Conclusions and Discussion

In this work, the dual effects of initial CAPE and concentration of aerosols acting as CCN on storm-scale microphysics, electrification and lightning discharges have been examined employing the WRF model coupled with a 2-moment microphysics parameterization and an explicit charging scheme. Our results indicate that the dynamic properties of storms are considerably influenced by the values of the CAPE, and that storms developing in conditions of higher CAPE produce more accumulated precipitation.

Under the same thermodynamic profile, the effects of increasing CCN concentration exhibit an increased cloud droplet concentration and a decreased droplet radius. It leads to the decrease in droplet self-collision and a delay in the formation of rain. These small droplets are transported by updrafts, and riming (i.e., ice-water collisions) will be intensified due to the increased supercooled CWC. The latent heat released from condensation and freezing supports the greater hydrometeor mass within updrafts. The aerosol impacts on these microphysical processes are consistent across the range of CAPE.

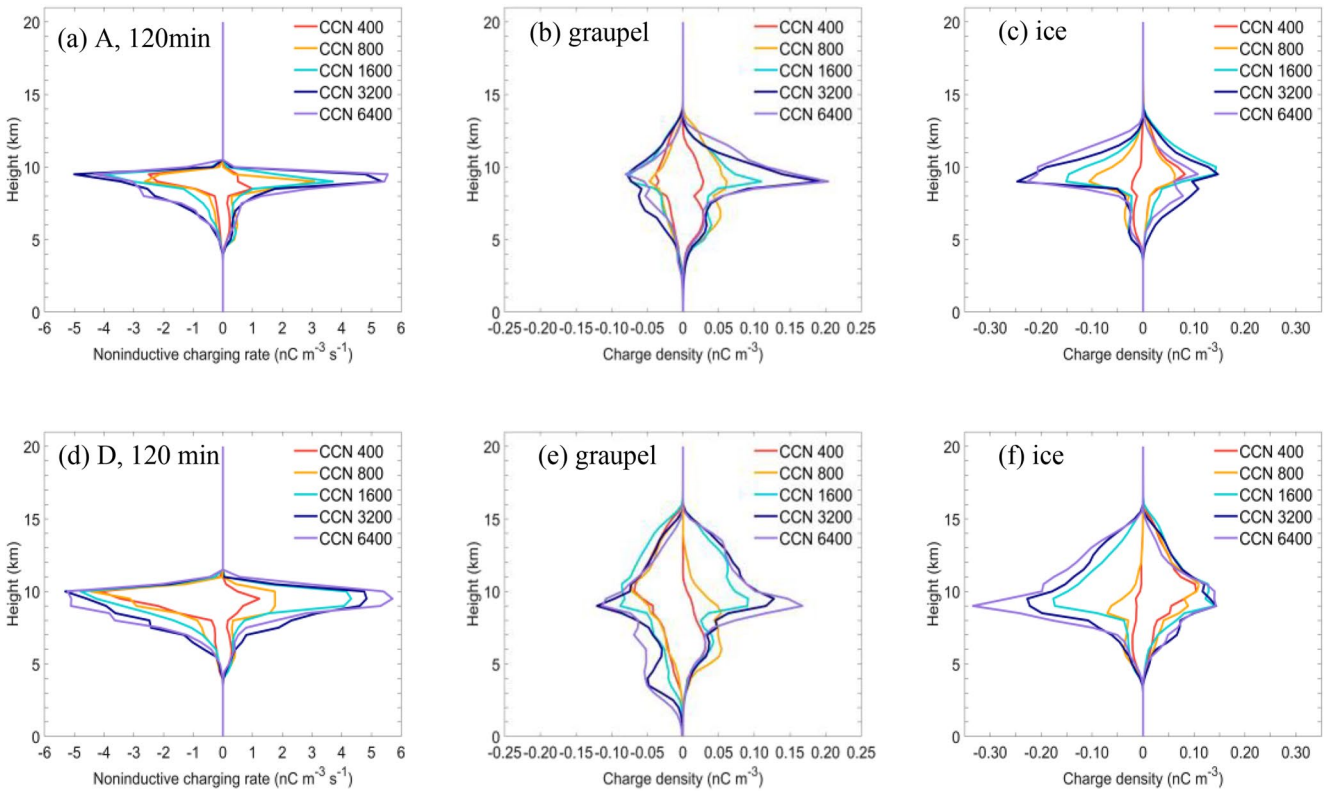

Figure 15. Vertical profiles of (a, d) peak non-inductive charging rates (pC m^{-3} s^{-1}), (b, e) peak charge density (nC m^{-3}) of graupel particle, and (c, f) peak charge density (nC m^{-3}) of ice crystal for the different surface mixing ratio conditions at the mature stage (120 min). (a–c) A, (d–f) D. The red, orange, blue, navy blue and purple lines correspond to the different cloud condensation nuclei concentrations of 400, 800, 1,600, 3,200, and 6,400 cm^{-3}.

The properties of graupel particles are determined jointly by the available aerosol concentration and the CAPE. They have counteracting effects on the graupel content and size. The graupel contents are greater at higher CAPE owing to larger precipitable water (more available vapor for condensation), while the graupel mass is reduced under polluted conditions via lower precipitation efficiency (mass diverted to anvil outflow). In the low CAPE environments, although the graupel mixing ratio is lower, the radius of graupel is noticeably larger under polluted conditions owing to the much lower number concentration. To some extent, the development of microphysical processes is promoted by the elevated aerosol loading, due to the larger size of graupel involved in charge separation. Owing to the increase in supercooled CWC, graupel charges more positively, and a charge structure with a negative charge region in upper levels appears because of the negatively charged ice crystals. Higher collision rates between ice-phase particles brings about the enhancement of charge separation and lightning formation. With the increase of CAPE value, the ice crystal content and charging rates increases significantly. While the graupel radius decreases slightly due to the increased graupel concentration, the larger ice crystal content ensures a more active non-inductive electrification. These yield a much higher charge density, leading to E_{mag} exceeding the specific breakdown value, ultimately culminating in higher lightning flash rates, compared to the low CAPE conditions.

Recent studies have shown that added aerosol concentration significantly boosts the lightning discharges in deep convective environments (Liu et al., 2021; Qie et al., 2021; Wang et al., 2018). Some observations have suggested that augmentation of total ice contents and robust mixed-phase processes under polluted conditions eventually lead to higher lightning flash rates (Liu et al., 2021; Zhao et al., 2020). Meanwhile, larger CAPE and mid-level RH also help to intensify lightning activity (Liu et al., 2011; Lu et al., 2022; Wang et al., 2018). The tangled influences of aerosol forcing and dynamics-thermodynamic effects on electrification are still poorly understood based on convection-resolved model simulation. In this study, we found that high CAPE significantly reinforced the non-inductive charging, and fueled more lightning flash rates. Under low CAPE conditions, the charge separation was enhanced even with smaller ice crystals content, mainly due to the increasing ice collisions resulting from

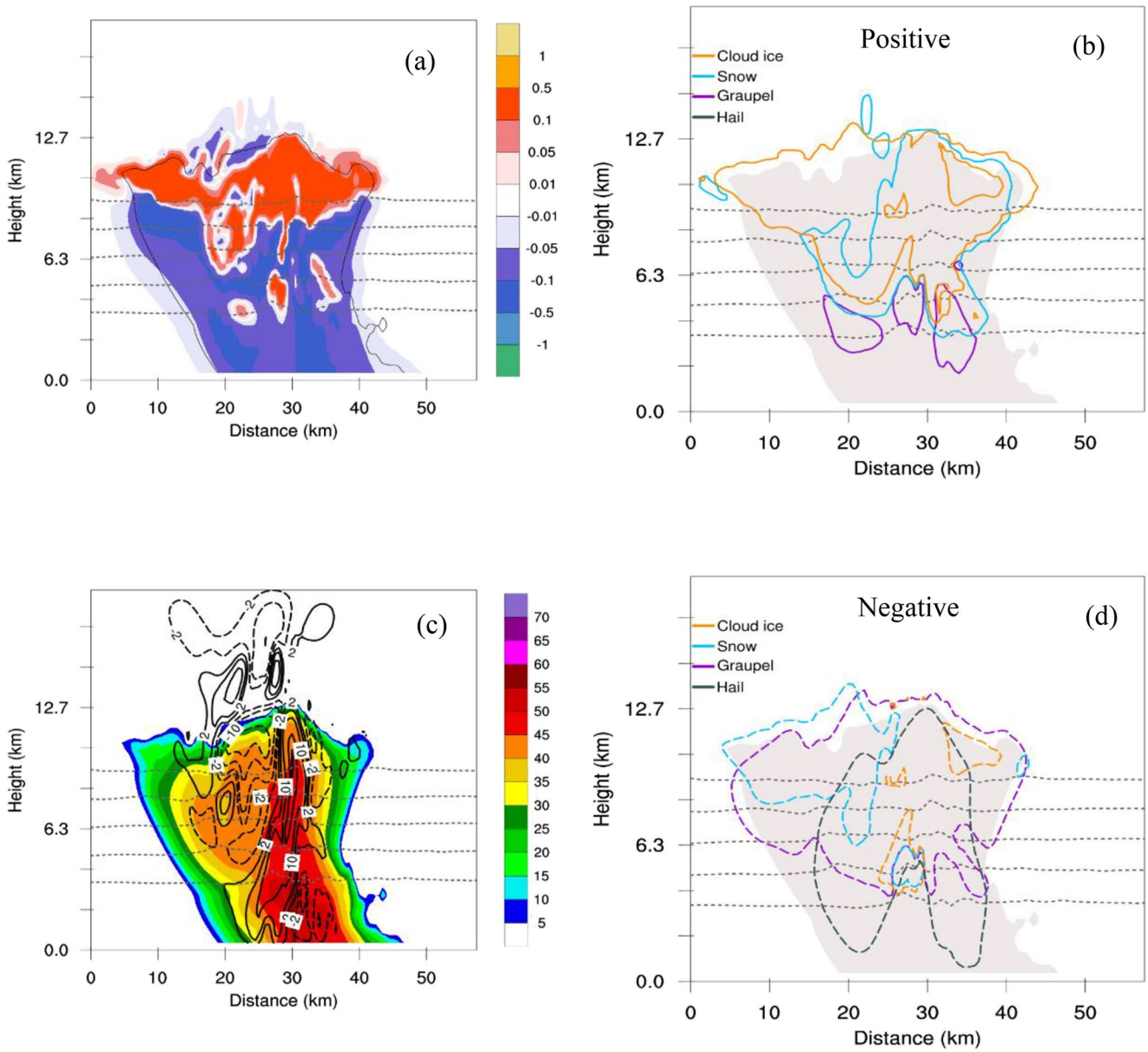

Figure 16. Vertical cross sections (northeast to southwest) at the location shown in Figure 2d of simulated variables at 120 min for case A-400. (a) Total net space charge (nC m^{-3}, shaded). The 0°C, −10°C, −20°C, −30°C and −40°C isotherms are shown by dashed gray lines in (a–d). (b) +0.1 nC m^{-3} space charge density contours for cloud ice (orange), graupel (purple), snow (blue), and hail (black). The cloud outline (reflectivity echoes ≥5 dBZ) is denoted by the gray shaded contour. (c) Radar reflectivity (unit: dBZ), black lines for vertical velocities (solid line: 2, 5, 10, 20, 25 m s^{-1}; dashed line: −2 m s^{-1}). (d) As in (b), but for −0.1 nC m^{-3} charge density.

larger graupel at greater CCN concentrations. It is noted that the cloud dynamics are more sensitive to instability than to aerosol loading, which is also indicated by Fan et al. (2007) and Storer et al. (2010). The aerosol effects on electrification and lightning were found to be more sensitive in environments of lower CAPE. Additional tests have been conducted by warming the ambient profile in mid-levels to achieve similar initial CAPE value (Van Weverberg, 2013), which is more like a tropical environment. The trends in charging rate and lightning formation for increasing aerosol concentrations are not robust in this condition. The results for aerosol effects on electrification and lightning therefore may not necessarily extend to, for example, tropical environments (see Figures S7–S9 in Supporting Information S1).

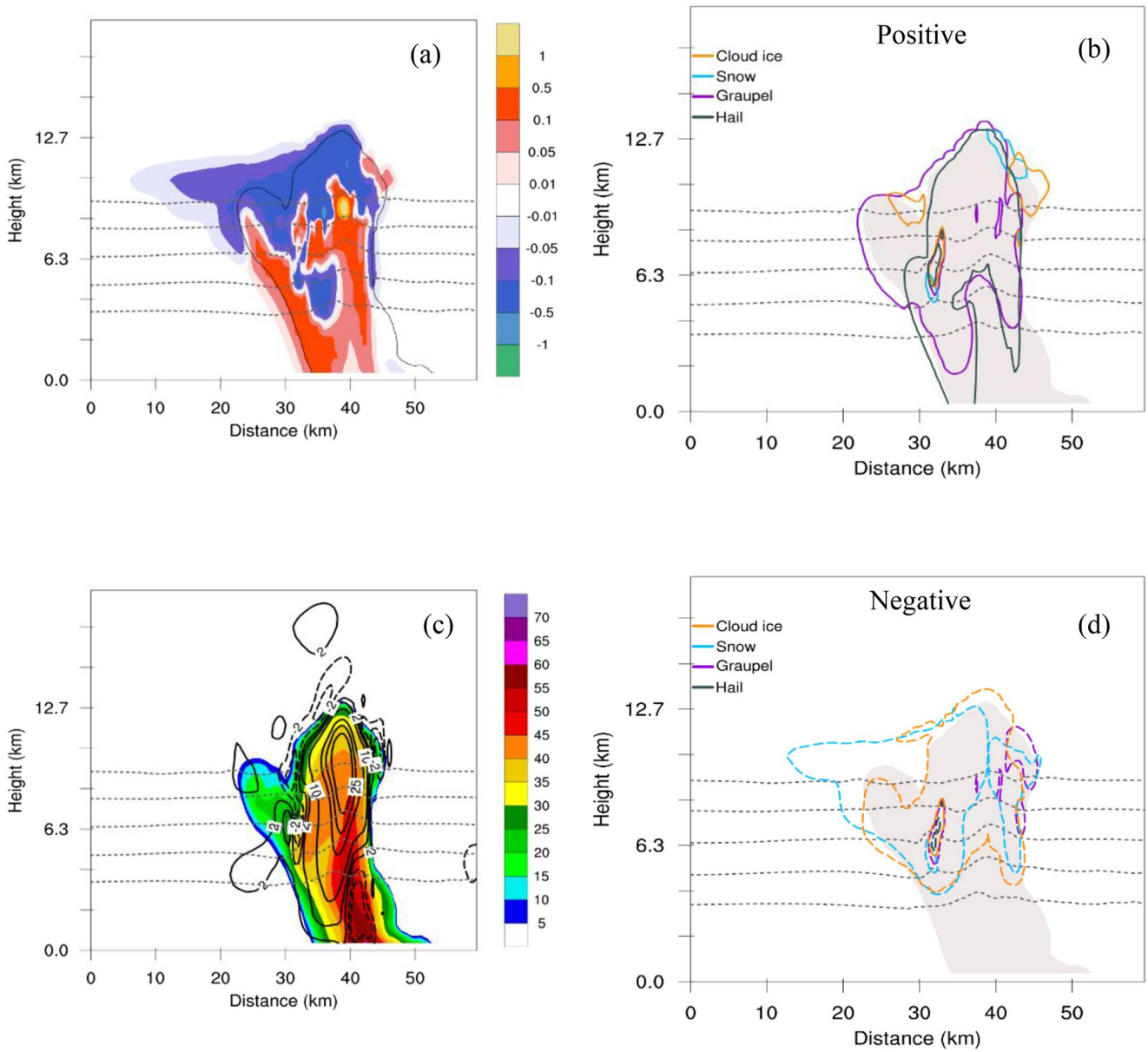

Figure 17. As in Figure 16, but the vertical cross sections for case A-6400.

It should be mentioned that our study only considered highly idealized model simulations, let alone more complex systems such as MCS or tropical cyclones. The impacts of aerosol concentration and instability on cloud microphysics and electrical processes can be distinct among different convective storms (Chen et al., 2020; Lee et al., 2017; Qie et al., 2020; Wu et al., 2013). More numerical simulations are still required to disentangle the detailed impacts of aerosol loading and dynamics-thermodynamics on electrification and lightning discharges with real case studies.

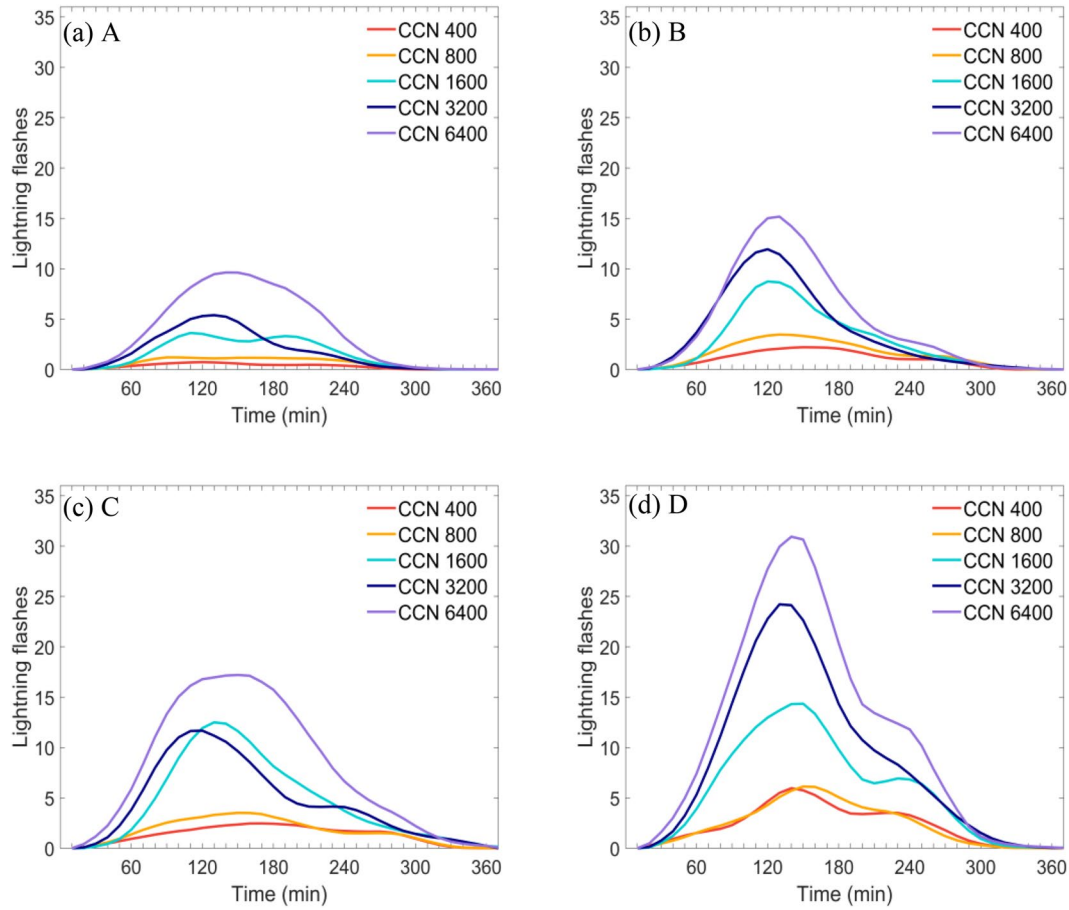

Figure 18. Temporal evolution of lightning flashes at the different surface mixing ratios. (a) A, (b) B, (c) C, (d) D. The red, orange, blue, navy blue and purple lines correspond to the different cloud condensation nuclei concentrations of 400, 800, 1,600, 3,200, and 6,400 cm^{-3}.

Data Availability Statement

This WRF-ELEC model (version 3.9.1) and the corresponding documentation are available at https://sourceforge.net/projects/wrfelec/ (Fierro et al., 2013; Mansell et al., 2010). The input data for the simulations can be found in the Zenodo repository (Sun et al., 2023).

Acknowledgments
This research was jointly supported by the National Natural Science Foundation of China (Nos. 42230609, 41630425, 41875007, 42030606), and the National Natural Science Foundation of China in collaboration with the Israel Science Foundation (Nos. 41761144074, 2640/17).

References

Altaratz, O., Koren, I., Yair, Y., & Price, C. (2010). Lightning response to smoke from Amazonian fires. *Geophysical Research Letters*, *37*(7), L07801. https://doi.org/10.1029/2010GL042679

Berg, W., L'Ecuyer, T., & van den Heever, S. (2008). Evidence for the impact of aerosols on the onset and microphysical properties of rainfall from a combination of satellite observations and cloud-resolving model simulations. *Journal of Geophysical Research*, *113*(D14), D14S23. https://doi.org/10.1029/2007JD009649

Bryan, G. H., Wyngaard, J. C., & Fritsch, J. M. (2003). Resolution requirements for the simulation of deep moist convection. *Monthly Weather Review*, *131*(10), 2394–2416. https://doi.org/10.1175/1520-0493(2003)131<2394:RRFTSO>2.0.CO;2

Chen, Q., Fan, J., Yin, Y., & Han, B. (2020). Aerosol impacts on mesoscale convective systems forming under different vertical wind shear conditions. *Journal of Geophysical Research*, *125*(3), e2018JD030027. https://doi.org/10.1029/2018JD030027

Dendy, J. E., Jr. (1987). Two multigrid methods for three-dimensional problems with discontinuous and anisotropic coefficients. *SIAM Journal on Scientific and Statistical Computing*, *8*(5), 673–685. https://doi.org/10.1137/0908059

Dwyer, J. R. (2003). A fundamental limit on electric fields in air. *Geophysical Research Letters*, *30*(20), 2055. https://doi.org/10.1029/2003GL017781

Dye, J. E., Knight, C. A., Toutenhoofd, V., & Cannon, T. W. (1974). The mechanism of precipitation formation in northeastern Colorado Cumulus III. Coordinated microphysical and radar observations and summary. *Journal of the Atmospheric Sciences*, *31*(8), 2152–2159. https://doi.org/10.1175/1520-0469(1974)031<2152:TMOPFI>2.0.CO;2

Eddy, A. J., MacGorman, D. R., Homeyer, C. R., & Williams, E. (2021). Intraregional comparisons of the near-storm environments of storms dominated by frequent positive versus negative cloud-to-ground flashes. *Earth and Space Science*, *8*(5), e2020EA001141. https://doi.org/10.1029/2020EA001141

Fan, J., Zhang, R., Li, G., & Tao, W. K. (2007). Effects of aerosols and relative humidity on cumulus clouds. *Journal of Geophysical Research*, *112*(D14), D14204. https://doi.org/10.1029/2006jd008136

Fierro, A. O., Mansell, E. R., MacGorman, D. R., & Ziegler, C. L. (2013). The implementation of an explicit charging and discharge lightning scheme within the WRF-ARW model: Benchmark simulations of a continental squall line, a tropical cyclone and a winter storm. *Monthly Weather Review*, *141*(7), 2390–2415. https://doi.org/10.1175/MWR-D-12-00278.1

Fierro, A. O., Rogers, R. F., Marks, F. D., & Nolan, D. S. (2009). The impact of horizontal grid spacing on the microphysical and kinematic structures of strong tropical cyclones simulated with the WRF-ARW Model. *Monthly Weather Review*, *137*(11), 3717–3743. https://doi.org/10.1175/2009MWR2946.1

Hu, J., Rosenfeld, D., Ryzhkov, A., Zrnic, D., Williams, E., Zhang, P., et al. (2019). Polarimetric radar convective cell tracking reveals large sensitivity of cloud precipitation and electrification properties to CCN. *Journal of Geophysical Research: Atmospheres*, *124*(22), 12194–12205. https://doi.org/10.1029/2019JD030857

Lee, S., Kim, B. G., Yum, S., Seo, K. H., Jung, C. H., Um, J. S., et al. (2017). Effects of aerosol on evaporation, freezing and precipitation in a multiple cloud system. *Climate Dynamics*, *48*(3–4), 1069–1087. https://doi.org/10.1007/s00382-016-3128-1

Li, G., Wang, Y., & Zhang, R. (2008). Implementation of a two-moment bulk microphysics scheme to the WRF model to investigate aerosol-cloud interaction. *Journal of Geophysical Research*, *113*(D15), D15211. https://doi.org/10.1029/2007JD009361

Li, Z., Wang, Y., Guo, J. P., Zhao, C. F., Cribb, M. C., Dong, X. Q., et al. (2019). East Asian study of tropospheric aerosols and their impact on regional clouds, precipitation, and climate (EAST-AIR(CPC)). *Journal of Geophysical Research: Atmospheres*, *124*(23), 13026–13054. https://doi.org/10.1029/2019jd030758

Liu, D., Qie, X., Xiong, Y., & Feng, G. (2011). Evolution of the total lightning activity in a leading-line and trailing stratiform mesoscale convective system over Beijing. *Advances in Atmospheric Sciences*, *28*(4), 866–878. https://doi.org/10.1007/s00376-010-0001-8

Liu, Y., Williams, E., Li, Z., Guha, A., Lapierre, J., Stock, M., et al. (2021). Lightning enhancement in moist convection with smoke-laden air advected from Australian wildfires. *Geophysical Research Letters*, *48*(11), e2020GL092355. https://doi.org/10.1029/2020GL092355

Lu, J., Qie, X., Xiao, X., Jiang, R., Mansell, E. R., Fierro, A. O., et al. (2022). Effects of convective mergers on the evolution of microphysical and electrical activity in a severe squall line simulated by WRF coupled with explicit electrification scheme. *Journal of Geophysical Research: Atmospheres*, *127*(16), e2021JD036398. https://doi.org/10.1029/2021JD036398

Lynn, B. H., Yair, Y., Shpund, J., Levi, Y., Qie, X., & Khain, A. (2020). Using factor separation to elucidate the respective contributions of desert dust and urban pollution to the 4 January 2020 Tel Aviv lightning and flash flood disaster. *Journal of Geophysical Research: Atmospheres*, *125*(24), e2020JD033520. https://doi.org/10.1029/2020JD033520

Mansell, E. R., MacGorman, D. R., Ziegler, C. L., & Straka, J. M. (2005). Charge structure and lightning sensitivity in a simulated multicell thunderstorm. *Journal of Geophysical Research*, *110*(D12), D12101. https://doi.org/10.1029/2004JD005287

Mansell, E. R., & Ziegler, C. L. (2013). Aerosol effects on simulated storm electrification and precipitation in a two-moment bulk microphysics model. *Journal of the Atmospheric Sciences*, *70*(7), 2032–2050. https://doi.org/10.1175/JAS-D-12-0264.1

Mansell, E. R., Ziegler, C. L., & Bruning, E. C. (2010). Simulated electrification of a small thunderstorm with two-moment bulk microphysics. *Journal of the Atmospheric Sciences*, *67*(1), 171–194. https://doi.org/10.1175/2009jas2965.1

Milbrandt, J. A., & Yau, M. K. (2005). A multimoment bulk microphysics parameterization. Part I: Analysis of the role of the spectral shape parameter. *Journal of the Atmospheric Sciences*, *62*(9), 3051–3064. https://doi.org/10.1175/JAS3534.1

Mitzeva, R., Latham, J., & Petrova, S. (2006). A comparative modeling study of the early electrical development of maritime and continental thunderstorms. *Atmospheric Research*, *82*(1–2), 26–36. https://doi.org/10.1016/j.atmosres.2005.01.006

Qie, K., Qie, X., & Tian, W. (2021). Increasing trend of lightning activity in the South Asia region. *Scientific Bulletin*, *66*(1), 78–84. https://doi.org/10.1016/j.scib.2020.08.033

Qie, X., Yuan, S., Chen, Z., Wang, D., Liu, D., Sun, M., et al. (2020). Understanding the dynamical-microphysical-electrical processes associated with severe thunderstorms over the Beijing metropolitan region. *Science China Earth Sciences*, *64*(1), 10–26. https://doi.org/10.1007/s11430-020-9656-8

Rosenfeld, D., Lohmann, U., Raga, G. B., O′Dowd, C. D., Kulmala, M., Fuzzi, S., et al. (2008). Flood or drought: How do aerosols affect precipitation. *Science*, *321*(5894), 1309–1313. https://doi.org/10.1126/science.1160606

Saunders, C. P. R., & Peck, S. L. (1998). Laboratory studies of the influence of the rime accretion rate on charge transfer during crystal/graupel collisions. *Journal of Geophysical Research*, *103*(D12), 13949–13956. https://doi.org/10.1029/97JD02644

Seifert, A., & Beheng, K. D. (2006). A two-moment cloud microphysics parameterization for mixed-phase clouds. Part 2: Maritime vs. continental deep convective storms. *Meteorology and Atmospheric Physics*, *92*(1-2), 67–82. https://doi.org/10.1007/s00703-005-0113-3

Skamarock, W. C., Klemp, J. B., Dudhia, J., Gill, D. O., Barker, D., Duda, M. G., et al. (2008). *A description of the advanced research WRF version 3 (No. NCAR/TN-475+STR)*. University Corporation for Atmospheric Research. https://doi.org/10.5065/D68S4MVH

Stolz, D. C., Rutledge, S. A., & Pierce, J. R. (2015). Simultaneous influences of thermodynamics and aerosols on deep convection and lightning in the tropics. *J. Geophys. Res.-Atmos.*, *120*(12), 6207–6231. https://doi.org/10.1002/2014JD023033

Storer, R. L., van den Heever, S. C., & Stephens, G. L. (2010). Modeling aerosol impacts on convective storms in different environments. *Journal of the Atmospheric Sciences*, *67*(12), 3904–3915. https://doi.org/10.1175/2010JAS3363.1

Sun, M., Liu, D., Qie, X., Mansell, E. R., Yair, Y., Fierro, A. O., et al. (2021). Aerosol effects on electrification and lightning discharges in a multicell thunderstorm simulated by the WRF-ELEC model. *Atmospheric Chemistry and Physics*, *21*(18), 14141–14158. https://doi.org/10.5194/acp-21-14141-2021

Sun, M., Qie, X., Mansell, E. R., Liu, D., Yair, Y., Fierro, A. O., et al. (2023). Aerosol impacts on storm electrification and lightning discharges under different thermodynamic environments. [Dataset]. Zenodo. https://doi.org/10.5281/zenodo.7536899

Takahashi, T. (1978). Riming electrification as a charge generation mechanism in thunderstorms. *Journal of the Atmospheric Sciences*, *35*(8), 1536–1548. https://doi.org/10.1175/1520-0469(1978)035<1536:REAACG>2.0.CO;2

Takahashi, T. (1984). Thunderstorm electrification—A numerical study. *Journal of the Atmospheric Sciences*, *41*(17), 2541–2558. https://doi.org/10.1175/1520-0469(1984)041<2541:TENS>2.0.CO;2

Thomas, R. J., Krehbiel, P. R., Rison, W., Hamlin, T., Harlin, J., & Shown, D. (2001). Observations of VHF source powers radiated by lightning. *Geophysical Research Letters*, *28*(1), 143–146. https://doi.org/10.1029/2000GL011464

Thornton, J. A., Virts, K. S., Holzworth, R. H., & Mitchell, T. P. (2017). Lightning enhancement over major oceanic shipping lanes. *Geophysical Research Letters*, *44*(17), 9102–9111. https://doi.org/10.1002/2017GL074982

Twomey, S. (1959). The nuclei of natural cloud formation, Part II: The supersaturation in natural clouds and the variation of cloud droplet concentration. *Geofisica pura e applicata*, *43*(1), 243–249. https://doi.org/10.1007/BF01993560

Van Weverberg, K. (2013). Impact of environmental instability on convective precipitation uncertainty associated with the nature of the rimed ice species in a bulk microphysics scheme. *Monthly Weather Review*, *141*(8), 2841–2849. https://doi.org/10.1175/MWR-D-13-00036.1

Wang, Q., Li, Z., Guo, J., Zhao, C., & Cribb, M. (2018). The climate impact of aerosols on the lightning flash rate: Is it detectable from long-term measurements? *Atmospheric Chemistry and Physics*, *18*(17), 12797–12816. https://doi.org/10.5194/acp-18-12797-2018

Weisman, M. L., & Klemp, J. B. (1984). The structure and classification of numerically simulated convective stormsin directionally varying wind shears. *Monthly Weather Review*, *112*(12), 2479–2498. https://doi.org/10.1175/1520-0493(1984)112<2479:TSACON>2.0.CO;2

Weisman, M. L., & Klemp, J. B. (1982). The dependence of numerically simulated convective storms on vertical wind shear and buoyancy. *Monthly Weather Review*, *110*(6), 504–520. https://doi.org/10.1175/1520-0493(1982)110<0504:TDONSC>2.0.CO;2

Westcott, N. E. (1995). Summertime cloud-to-ground lightning activity around major Midwestern urban areas. *Journal of Applied Meteorology*, *34*(7), 1633–1642. https://doi.org/10.1175/1520-0450-34.7.1633

Williams, E. R., Mushtak, V., Rosenfeld, D., Goodman, S., & Boccippio, D. (2005). Thermodynamic conditions favorable to superlative thunderstorm updraft, mixed phase microphysics and lightning flash rate. *Atmospheric Research*, *76*(1–4), 288–306. https://doi.org/10.1016/j.atmosres.2004.11.009

Wu, X., Qie, X., & Yuan, T. (2013). Regional distribution and diurnal variation of deep convective systems over the Asian monsoon region. *Science China Earth Sciences*, *56*(5), 843–854. https://doi.org/10.1007/s11430-012-4551-8

Yair, Y., Lynn, B., Price, C., Kotroni, V., Lagouvardos, K., Morin, E., et al. (2010). Predicting the potential for lightning activity in Mediterranean storms based on the Weather Research and Forecasting (WRF) model dynamic and microphysical fields. *Journal of Geophysical Research*, *115*(D4), D04205. https://doi.org/10.1029/2008JD010868

Yair, Y., Lynn, B., Yaffe, M., Ziv, B., & Shpund, J. (2021). Observations and numerical simulations of the October 25th, 2015 super-cell thunderstorm over Central Israel. *Atmospheric Research*, *247*, 105165. https://doi.org/10.1016/j.atmosres.2020.105165

Yuan, T. L., Remer, L. A., Pickering, K. E., & Yu, H. B. (2011). Observational evidence of aerosol enhancement of lightning activity and convective invigoration. *Geophysical Research Letters*, *38*(4), L04701. https://doi.org/10.1029/2010GL046052

Zhao, P., Li, Z., Xiao, H., Wu, F., Zheng, Y., Cribb, M. C., et al. (2020). Distinct aerosol effects on cloud-to-ground lightning in the plateau and basin regions of Sichuan, Southwest China. *Atmospheric Chemistry and Physics*, *20*(21), 13379–13397. https://doi.org/10.5194/acp-20-13379-2020

Zhao, Z., Qie, X., Zhang, T., Zhang, T., Zhang, H., Wang, Y., et al. (2010). Electric field soundings and the charge structure within an isolated thunderstorm. *Chinese Science Bulletin*, *55*(9), 872–876. https://doi.org/10.1007/s11434-009-0471-1

Ziegler, C. L. (1985). Retrieval of thermal and microphysical variables in observed convective storms. Part 1: Model development and preliminary testing. *Journal of the Atmospheric Sciences*, *42*(14), 1487–1509. https://doi.org/10.1175/1520-0469(1985)042<1487:ROTAMV>2.0.CO;2

Ziegler, C. L., & MacGorman, D. R. (1994). Observed lightning morphology relative to modeled space charge and electric field distributions in a tornadic storm. *Journal of the Atmospheric Sciences*, *51*(6), 833–851. https://doi.org/10.1175/1520-0469(1994)051<0833:OLMRTM>2.0.CO;2

Zrnic, D. S., Balakrishnan, N., Ziegler, C. L., Bringi, V. N., Aydin, K., & Matejka, T. (1993). Polarimetric signatures in the stratiform region of a mesoscale convective system. *Journal of Applied Meteorology*, *32*(4), 678–693. https://doi.org/10.1175/1520-0450(1993)032<0678:PSITSR>2.0.CO;2

References From the Supporting Information

Bruning, E. C., Rust, W. D., Schuur, T. J., MacGorman, D. R., Krehbiel, P. R., & Rison, W. (2007). Electrical and polarimetric radar observations of a multicell storm in TELEX. *Monthly Weather Review*, *135*(7), 2525–2544. https://doi.org/10.1175/MWR3421.1